Risk assessment of the Groningen geothermal potential

Daniilidis, Alexandros; Doddema, Leon; Herber, Rien

Published in:
Geothermics

DOI:
10.1016/j.geothermics.2016.06.014

Publication date:
2016

Geothermics 64 (2016) 271–288

Contents lists available at ScienceDirect

Geothermics

journal homepage: www.elsevier.com/locate/geothermics

Risk assessment of the Groningen geothermal potential: From seismic to reservoir uncertainty using a discrete parameter analysis

Alexandros Daniilidis*, Leon Doddema, Rien Herber

University of Groningen, Energy and Sustainability Research Institute Groningen (ESRIG), Geo-Energy Group, Nijenborgh 4, P.O. Box 800, 9747 AG, Groningen, The Netherlands

ARTICLE INFO

Article history:
Received 12 October 2015
Received in revised form 15 June 2016
Accepted 22 June 2016
Available online 7 July 2016

Keywords:
Geothermal
3D reservoir model
Pressure depletion
Uncertainty
Rotliegend
Risk assessment

ABSTRACT

Geothermal exploitation is subject to several uncertainties, even in settings with high data availability, adding to project risk. Uncertainty can stem from the reservoir's initial state, as well as from the geological and operational parameters. The interplay between these aspects entails irreducible risk prior to exploration drilling. Consequently it is difficult to construct an indicative qualitative and quantitative depiction of the most prominent facets (e.g. pressure, permeability). This paper shows the classification of known unknowns to risks, while also providing numerical results. Starting from seismic data and arriving at a reservoir model using a discrete parameter analysis we assess the risks and uncertainties of a geothermal project near the city of Groningen (NE Netherlands). By simulating all combinations of the considered parameters, their relative importance can be mapped out. Findings suggest that the unique regime of possible pressure depletion due to neighbouring gas production can highly impact the feasibility of the project. Results demonstrate how an in depth analysis at the exploration phase can direct future efforts towards the most significant elements. Although the numerical results are field specific, the methodology can be readily applied to different locations.

1. Introduction

The municipality of Groningen has the ambition to realize a deep geothermal development as part of their CO_2 neutrality agenda for 2030. The geothermal source is envisioned as the baseload component of a heat network, serving some 10,000 households. The Permian Rotliegend sandstone is considered as the target aquifer with a proven good reservoir quality, as demonstrated by the nearby Groningen gas field. Based on a preliminary evaluation an exploration license has been awarded to the municipality in 2011 (Fig. 1). Top reservoir depth of the Rotliegend Slochteren (ROSL) sandstone within the license is ca. 3400 m, with an average thickness of ca. 250 m.

Despite the good 3D seismic coverage and regional well control, some of the critical parameters for the performance of the geothermal doublet (e.g. permeability, pressure, compartmentalization, gas saturation) will remain subject to various degrees of uncertainty, irreducible prior to drilling. Several studies have analysed the effect of uncertainties on geothermal output. For low enthalpy fields various aspects have been considered, namely rock thermal properties (Vogt et al., 2010; Mottaghy et al., 2011), rock properties together with well positioning (Vogt et al., 2013) and more recently flow rate, reservoir characteristics and temperature, injection temperature and well spacing (Saeid et al., 2015). The impact of different parameter uncertainties on power output has also been showcased analytically (van Wees et al., 2012). Pressure profiles in particular are known to present difficulties for accurate simulation (Franco and Vaccaro, 2014).

Methodologically different approaches are applied to capture uncertainty, such as Monte Carlo (Mottaghy et al., 2011; Vogt et al., 2010; Vogt et al., 2013) and parameter analysis (Poulsen et al., 2015; Saeid et al., 2015). Reservoir simulation models are either based on a geological model (Mottaghy et al., 2011; Vogt et al., 2013) or use a representative geometry and a homogeneous, constant thickness reservoir (Saeid et al., 2015).

Five decades of gas production from the Groningen field have resulted in pressure depletion in the field itself and the aquifer in its surroundings (Breunese and van Thienen-Visser, 2014; TNO, 2014). Furthermore some dissolved gas is also expected to be present in the targeted reservoir. To the best of our knowledge, the joint effect of uncertainty in initial pressure and gas saturation in geothermal doublet performance has not been investigated before.

Thus, this study focuses on the risk assessment of a low-enthalpy geothermal doublet in a Rotliegend aquifer, with consideration of the uncertainties at three different levels: initial aquifer state (pressure depletion and gas saturation), reservoir (rock and fault

* Corresponding author.
E-mail address: a.daniilidis@rug.nl (A. Daniilidis).

http://dx.doi.org/10.1016/j.geothermics.2016.06.014
0375-6505/

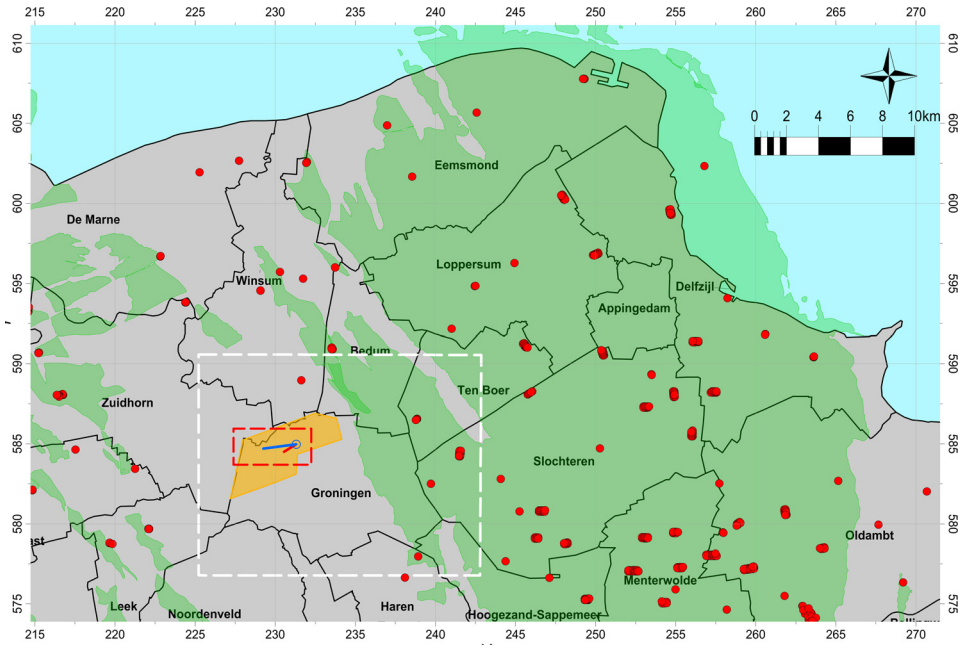

Fig. 1. Area of interest in the north of the Netherlands. Gas fields are plotted in green, the orange surface indicates the geothermal license, white rectangle indicates the extent of the interpreted 3D seismic cube and the red dashed rectangle outlines the reservoir model. Proposed well trajectories are indicated with blue (injector) and red (producer) lines. Red dots mark the location of existing gas wells, while aggregated dots indicate the presence of a cluster. Map coordinates are in RD. (For interpretation of the references to colour in this figure legend, the reader is referred to the web version of this article.)

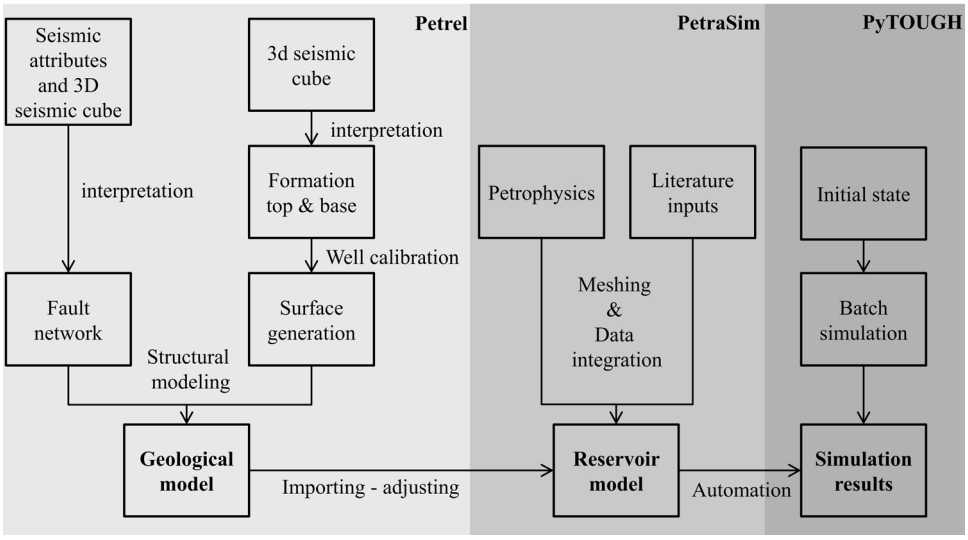

Fig. 2. Work flow chart overview of the methodology. The PetraSim and PyTOUGH parts are further substantiated in Fig. 7.

Table 1
Initial state main inputs. Other porosity values for faults were also considered (5% and 15%) but proved to have little effect on the results, therefore a middle value of 10% was used throughout the analysis. Wet heat conductivity and specific heat values are based on data from several sources (Ondrak et al., 1998; Muntendam-Bos et al., 2008; Schön, 2011). Reservoir layer porosity and permeability data are detailed in Table 2.

Lithological group	Density (kg/m^3)	Porosity (%)	Permeability (horizontal) (mD)	Wet heat conductivity (W/m*K)	Specific heat (J/kg*K)
Zechstein salt (overburden)	2170	1	10^{-10}	3.5	1050
Rotliegend (reservoir)	2500–2700	variable	variable	2.9	827
Limburg (basement)	2900	1	10^{-2}	2.65	840
Faults	2800	10	variable	2.9	827

permeability) and lastly operational (flow rate and re-injection temperature) parameters. A comprehensive discrete parameter analysis makes it possible to consider all potential parameter combinations, analyzing the interaction between them through a numerical model. With this approach the amount of data and simulation time needed is reduced compared to a full Monte Carlo simulation. Furthermore, the analysis is based on a realistic reservoir geometry derived from interpretation of 3D seismic data.

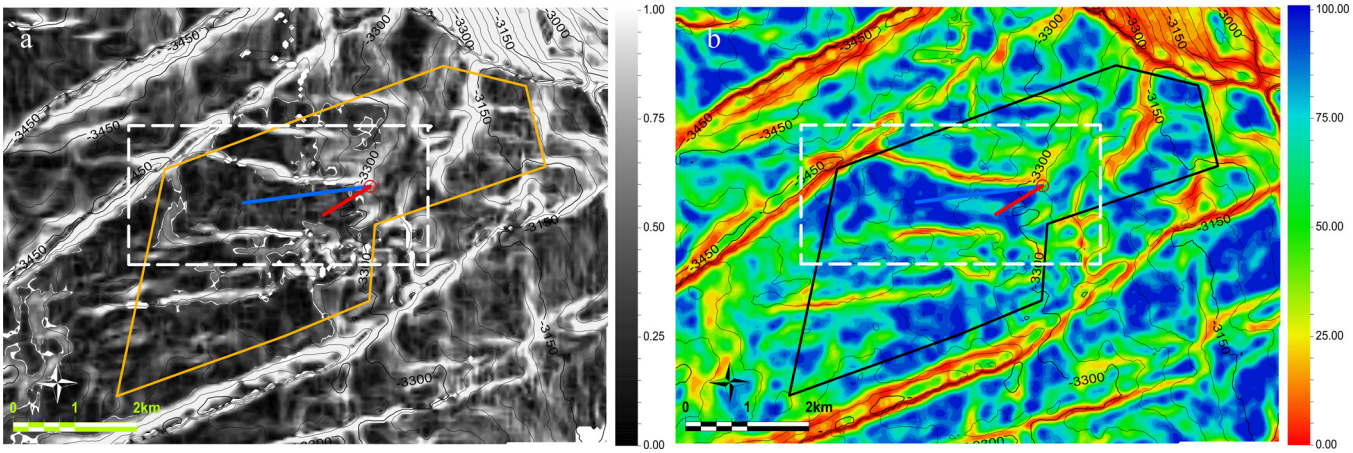

Fig. 3. Dip illumination (a) and edge detection (b) attributes along the top reservoir surface. Dip illumination reveals signal discontinuities and noisy areas. It uses a gradient decent and dip estimation to compute volume curvature attributes. A search window of 20 m with a zero offset was used without a direction. Edge detection highlights surface areas with subtle changes in topography and helps identify discrete sharp edges. This is achieved by a combination of dip and azimuth that is normalized to the noise surface of the signal. Both attributes highlight the fault patterns at top Rotliegend level. The white dotted rectangle outlines the extent of the reservoir model.

2. Geological setting and background

The Netherlands is situated in the Southern Permian Basin which has been extensively studied for hydrocarbons (Doornenbal et al., 2010; van Ojik et al., 2011), based on a very large number of wells and seismic surveys (de Jager and Geluk, 2007; Grötsch et al., 2011). The Groningen gas field is the largest in Europe, situated on the crest of the Groningen structural high (de Jager, 2007; Ligtenberg et al., 2011), at depths ranging between ca. 2800 m and 3000 m (Grötsch et al., 2011). Its presence has led to an extensive exploration of the structural highs in the area, supported by numerous geological, structural and geophysical studies (Grötsch et al., 2011). The largest part of the gas reserves (more than 90%) of the Groningen gas field was generated by Westphalian coals and Carboniferous shales (Laier et al., 1997; van Gent et al., 2009). The gas is trapped in the Permian Rotliegend sandstone reservoir, sealed by Zechstein evaporites which have been subjected to halokinesis (de Jager and Geluk, 2007; van Gent et al., 2009). The Rotliegend lithostratigraphy is the result of retreats and advances of desert lake systems in several cycles, reworked by aeolian sands (Fryberger et al., 2011; van Ojik et al., 2011). The range of depositional environments broadens towards the North and includes fluvial, aeolian, playa and lacustrine facies (McKie, 2011).

Despite the extensive exploration for gas, the use of the Rotliegend sandstone in the Netherlands for geothermal applications is not widespread. The only project in the North Netherlands region Koekoekspolder, that targeted the Rotliegend sandstone in aeolian dune facies, encountered lower than expected thickness, net-to-gross and permeability values (Henares et al., 2014), the latter attributed to anhydrite cementation.

The Groningen geothermal concession area is located in the Lauwerszee Trough at the western margin of the gas field. It covers a graben of Rotliegend sandstone in fluvial/sabkha facies, surrounded by structural highs, many of which are gas-bearing. Hydrostatic pressure and temperature gradients in the region are well understood (Verweij et al., 2011; Bonté et al., 2012). Nonetheless, the Groningen gas field has been producing since 1963 (Grötsch et al., 2011), resulting in pressure depletion in the field and surround-

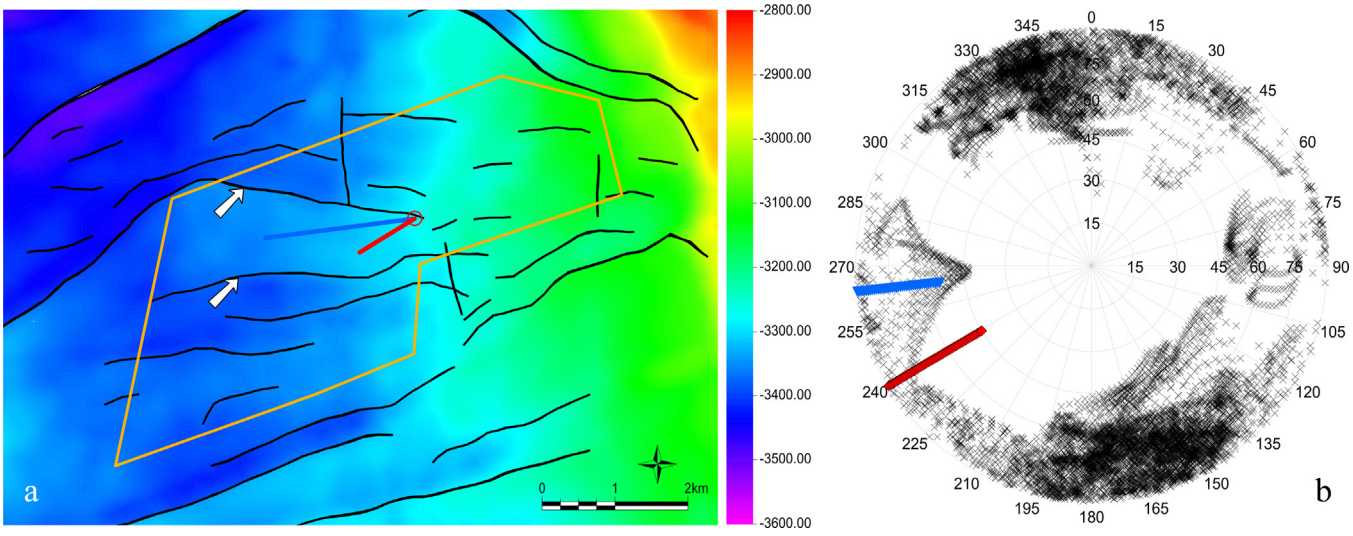

Fig. 4. (a) top reservoir depth map with fault traces represented by black lines, license area in orange and injector and producer in blue and red respectively. The dominant orientation is NE-SW followed by NW-SE, while a few smaller faults show a roughly E-W orientation. The white arrows mark the two major bounding faults of the reservoir that were included in the simulations. (b) stereonet window with dip and azimuth of regularly sampled points on the 3D fault surfaces around the concession. Most faults display a dip angle between 90° and 60°. Black marks represent points on fault surfaces while red and blue points represent producer and injector respectively. (For interpretation of the references to colour in this figure legend, the reader is referred to the web version of this article.)

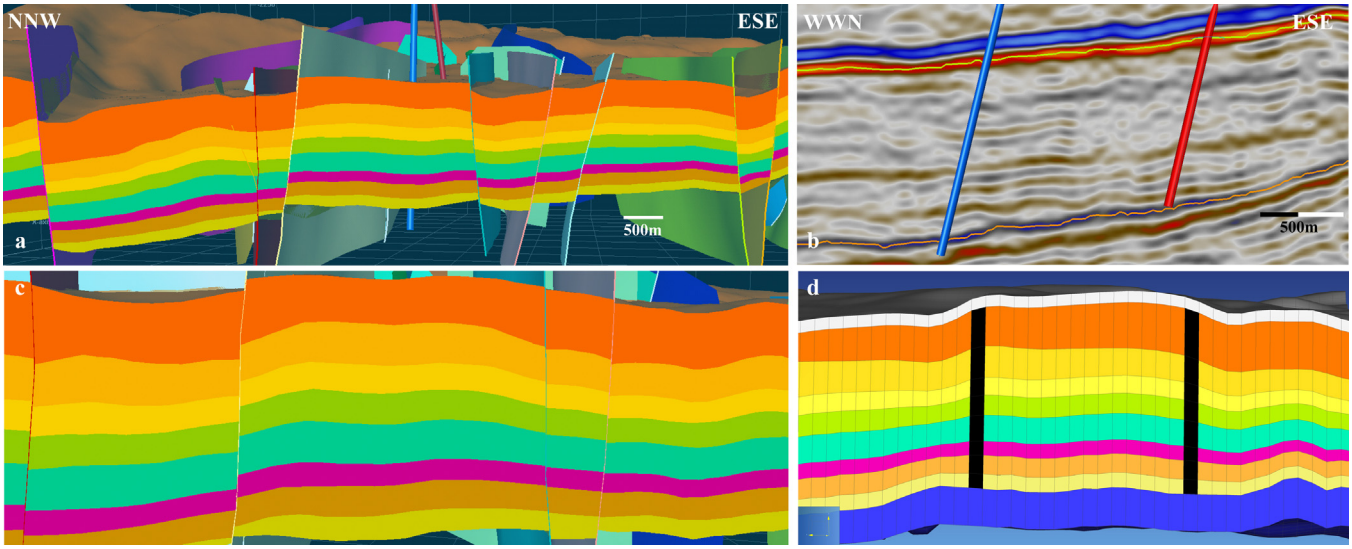

Fig. 5. (a) geological model of the reservoir, view from W-SW, (b) seismic line along the well plane inside the reservoir. Top reservoir is interpreted in green and the Saalian unconformity in orange. Wells are highlighted in blue (injector) and red (producer) for both figures, (c) close up of the targeted block and (d) the reservoir model of the geological model from (c). (For interpretation of the references to colour in this figure legend, the reader is referred to the web version of this article.)

ings (Breunese and van Thienen-Visser, 2014; TNO, 2014). Pressure depletion and accompanying reservoir compaction and subsidence have been identified as the governing processes of recent seismicity events in the region (Van Wees et al., 2014; van Thienen-Visser and Breunese, 2015).

The extent to which pressure depletion propagates through the aquifer beyond the gas field is not well understood, making the pressure levels within the license area uncertain. The pressure regime can therefore be expected to range between hydrostatic (340–350 bar) and a depletion down to 115 bar (current pressure level of the gas field, NAM personal communication 2015). Furthermore, due to proximity to the Groningen and smaller gas fields and the presence of the underlying carboniferous source rock, the aquifer in the considered reservoir target could hold amounts of gas (NLOG, 2015). The percentage of gas in the reservoir remains uncertain but is expected to be mostly dissolved.

Geological uncertainty does not only relate to reservoir quality and characteristics, but also to the sealing or non-sealing nature of the faults which are abundantly present in the area. Some faults are documented to act as flow barriers thus compartmentalizing the Rotliegend reservoirs (Leveille et al., 1997; Van Hulten, 2010; Ligtenberg et al., 2011). Lastly, the effect of the operating conditions and their prediction is essential for designing a geothermal installation and its long term deployment (Franco and Vaccaro, 2014). Operating conditions (e.g. flow rate and re-injection temperature) for the Groningen project remain undecided at this point, adding to the uncertainty.

3. Methods

3.1. Overview

Our analysis employs a streamlined workflow from seismic data to reservoir parameter assessment, as depicted in Fig. 2. The Petrel software suite (Schlumberger, 2012) was used for seismic interpretation and geological modelling. The PetraSim software (Rockware, 2014) combined with PyTOUGH (Florian Wellmann et al., 2012; Croucher, 2014) scripts was used for the simulations. PetraSim makes use of the TOUGH2 code family that utilizes the finite difference method (Pruess, 1991). The EWASG (Equation-of-State for Water, Salt and Gas) equation of state module was chosen as the most suitable, as it can accommodate three components in the pore-fill mixture, namely water, salt and a non-condensable gas (e.g. CH_4) (Battistelli et al., 1997). The EWASG equation of state was setup to accommodate non-isothermal CH_4 gas in two phase flow with brine.

The inclusion of all combinations of discrete parameters deepens the understanding of their interrelation as opposed to varying one parameter at a time as in the work of Saeid et al. (2015). The focus is towards the reservoir potential and does not address well

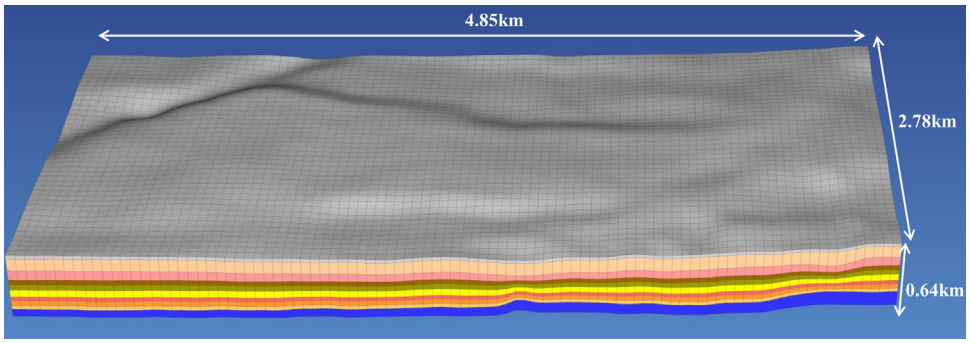

Fig. 6. Generalized initial state model architecture and dimensions. Grey and blue colors represent the overlying salt and underlying carboniferous basement respectively. Reservoir layers are represented by the other colors. (For interpretation of the references to colour in this figure legend, the reader is referred to the web version of this article.)

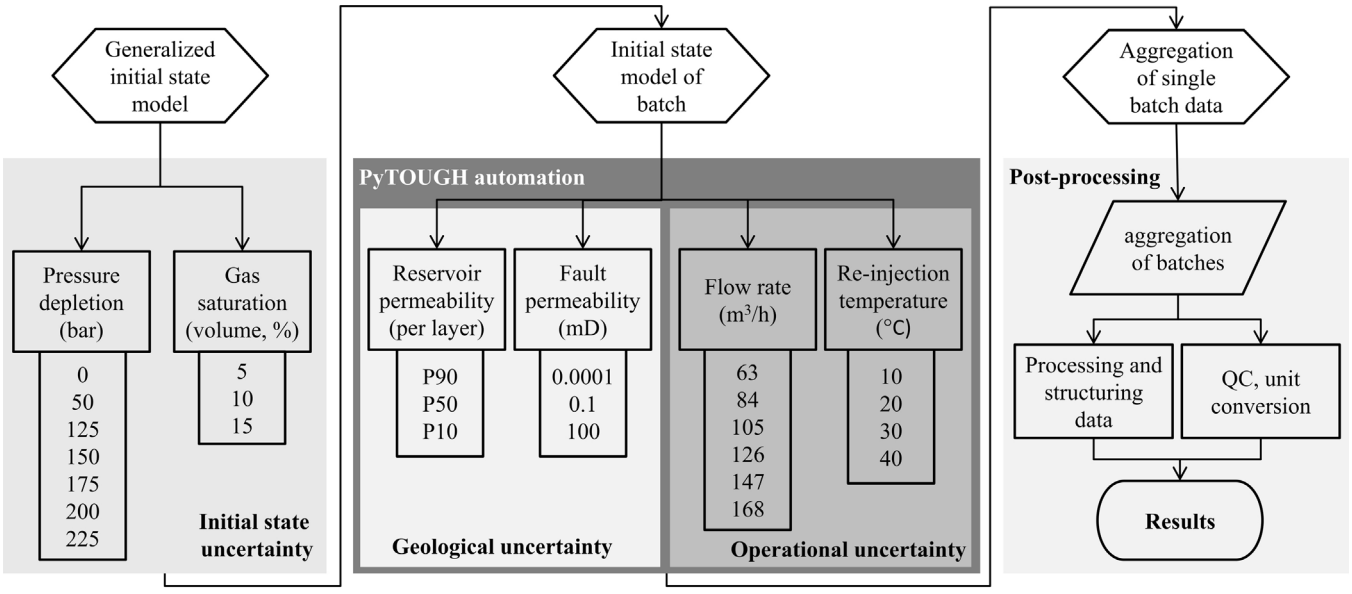

All combinations between the discrete values of pressure depletion and gas saturation are considered, amounting to **21** unique initial state batches

All combinations between the discrete values for geological (**9**) and operational uncertainty (**24**) are considered, amounting to **216** unique simulations per batch.

With **21** unique initial state batches and **216** unique simulations per batch, results include a total of **4536** unique reservoir simulations

Fig. 7. Discrete steps followed for the reservoir simulation workflow. Due the amount of data produced by the simulations, only the results on the injector and producer cells were stored and are included in the results.

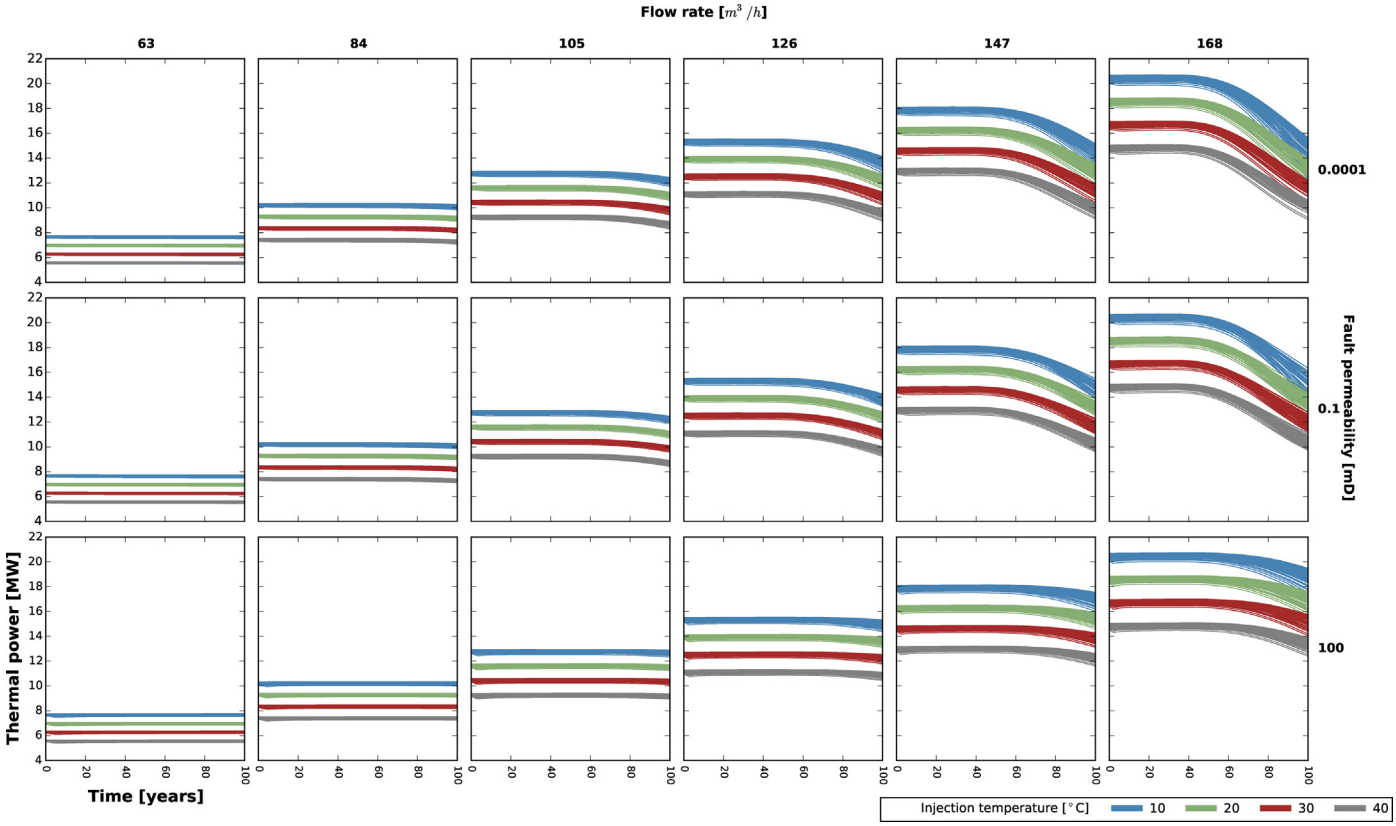

Fig. 8. Thermal power output (MW) as a function of time, flow rate, fault permeability and injection temperature. "Spread" between the injection temperature effect increases with higher flow rates. Breakthrough occurs sooner (curves bend) with higher flow rates and sealing faults. Permeable faults extend the lifetime of the system.

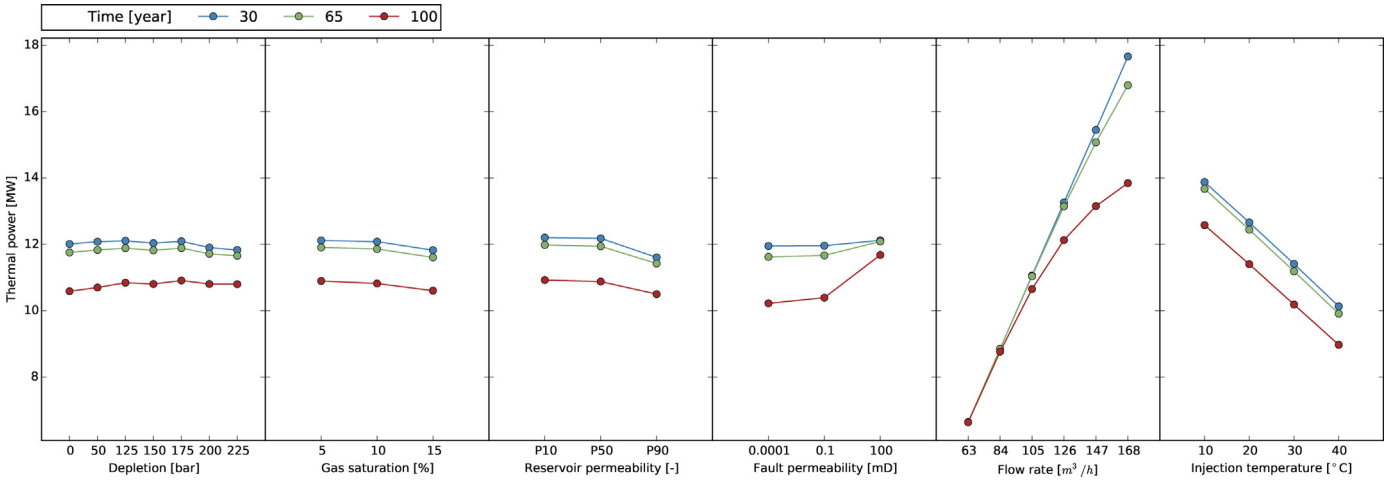

Fig. 9. Mean values of thermal output (MW) for all uncertainty classes. The co-dependency of the variables causes the mean values presented to be different (lower) than the absolute values of the individual simulations presented in Fig. 8.

bore effects. Well geometry and trajectories are the same for all simulations.

3.2. Geological data

3.2.1. Seismic interpretation

A 3D Pre-Stack Depth Migrated (PSDM) seismic cube from NAM (Nederlandse Aardolie Maatschappij BV) was used to interpret the main stratigraphic units in the area. The dimensions of the cube are 17.5 km (N-S) by 13.7 km (E-W) by 4 km (depth). The inline and crossline interval of the seismic data is 25m. Interpretation was carried out every 8th line (200 m) in both directions.

The license area covers a surface of 17.9 km^2 where interpretation was carried out every 4th line (100 m) in both directions. Interpretation was calibrated with the 22 wells present inside the seismic cube area.[1]

Edge detection and dip illumination seismic attributes (Fig. 3) were used together with the original seismic cube to aid fault interpretation, shown in Fig. 4. The Saalian unconformity between the Carboniferous and the base of the overlying Rotliegend group was mapped after flattening the seismic at top Rotliegend. The resulting surfaces and fault planes served as input for the structural framework of the geological modelling.

The spatial distribution and strike azimuth of the interpreted faults on the top reservoir surface is depicted in Fig. 4a. Most faults have a NE-SW or NW-SE orientation, consistent with previous observations in the area (van Gent et al., 2009). The faults point cloud highlights the presence of sets of faults with conjugate azimuths, most of which show dip angles higher than 30° (Fig. 4b). The prevailing fault orientation suggests that N-S fault surfaces are less common. Therefore, sub-seismic resolution faults along the N-S axis between the wells are not likely to be present and well communication should not be affected.

3.2.2. Petrophysical data

Petrophysical data for poro-perm values were obtained from Panterra (van Leeuwen et al., 2014). Public data logs (gamma-ray, sonic, bulk density, bulk density correction, neutron porosity, caliper) from 8 wells (EKL-01, NRD-01, PSP-01, ROD-101, SSM-01, SSM-02, SAU-01, TBR-04) around the concession together with core measurements were used to infer layer characteristics within the target Rotliegend reservoir. Gross thickness, net sand, net-to-gross, porosity and P90-P50-P10 values of permeability per well and per layer were provided.

[1] Wells used for seismic interpretation: SAU-01, EKL-01 to EKL-13, HRS-01 to HRS-02-S2, TBR-01 to TBR-04

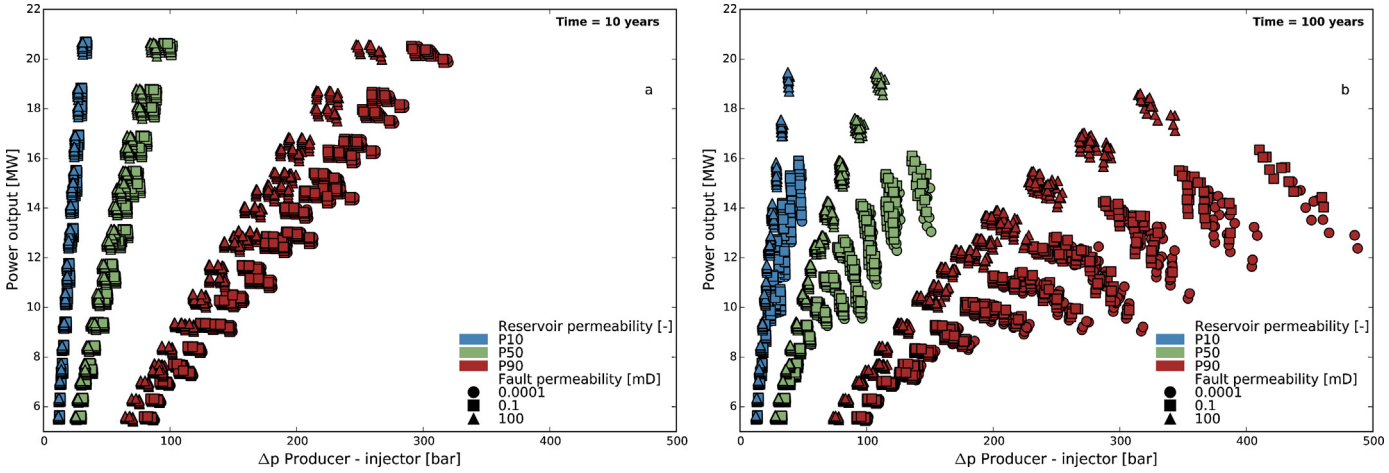

Fig. 10. Thermal power output against well producer and injector Δp, coded based on reservoir and fault permeability. Two different time interval are shown: 10 years (a) and 100 years (b). A video with a time series animation and a step of 1 year is digitally available.

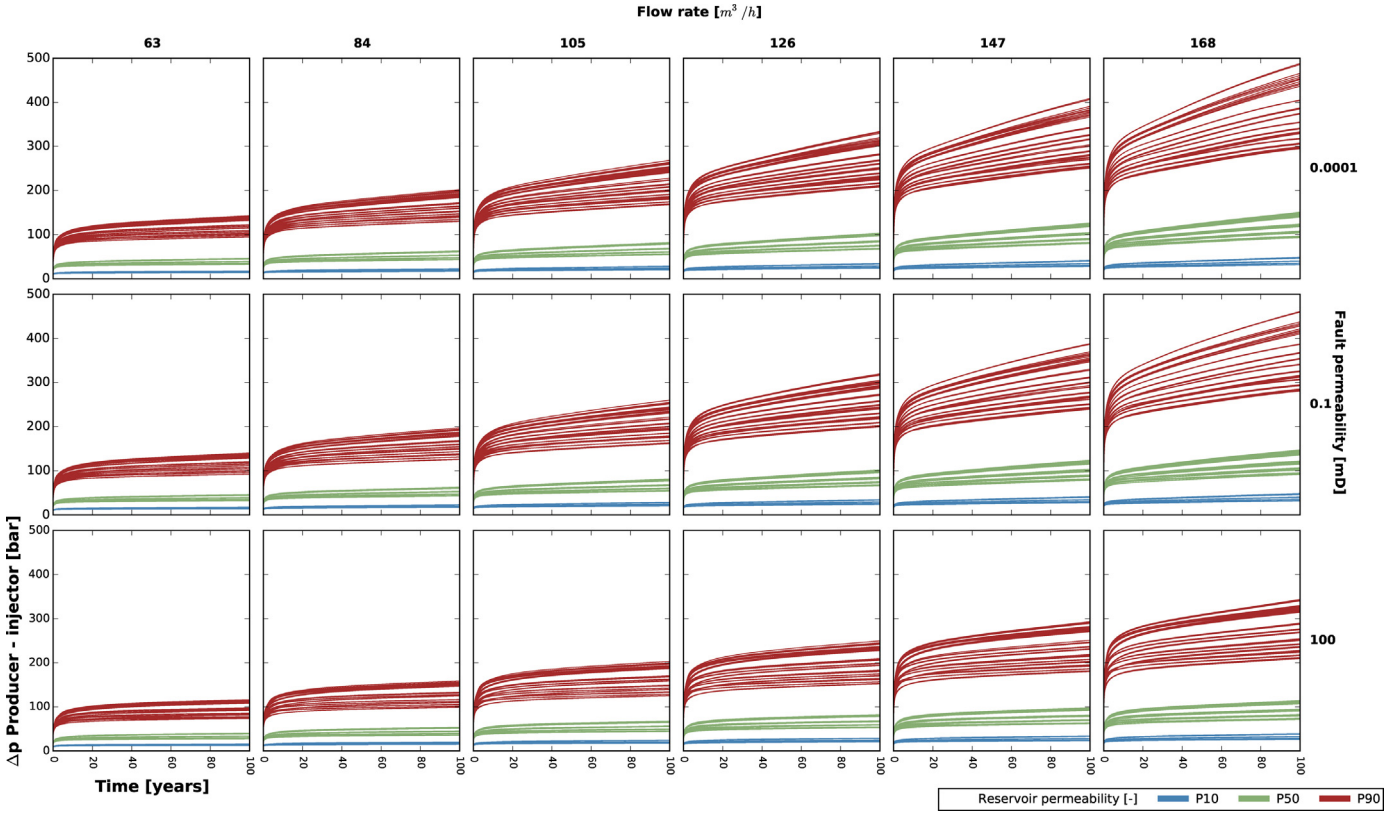

Fig. 11. Pressure difference between producer and injector as a function of time, flow rate, reservoir permeability and fault permeability.

The petrophysical data were aggregated with equal weights of 1 for the wells, except for the SAU-01 well which is most proximal (ca. 4 km) to the concession (weight factor 2). The lack of data for vertical permeability was accounted for in the model by consistently assigning a vertical permeability which was one order of magnitude lower than the respective horizontal permeability (Carlson, 2003). This is a worst case estimate compared to the Kx/Kz ratio of 1.7 usually used for the Rotliegend (van Leeuwen et al., 2014). Angled contacts between deviated wells and reservoir cells are therefore taken into account.

3.2.3. *Well location and trajectory*

Following the fault interpretation, fault planes were used to extract points with dip azimuth and dip angle of the fault surfaces. Using these data in relation to the faulted blocks in the license area, the targeted compartment was chosen together with a commercial project stakeholder (Well Engineering Partners, WEP). The objective of the well trajectories was to target the largest non-faulted block in the concession and ensure, as much as possible good communication between injector and producer wells (Fig. 4). WEP further designed well trajectories and casing schemes (Boersma and Brinkgreve, 2014). The producer well trajectory takes into account the possibility of encountering a depleted reservoir, which would require placing the pump deeper in the well. For this reason,

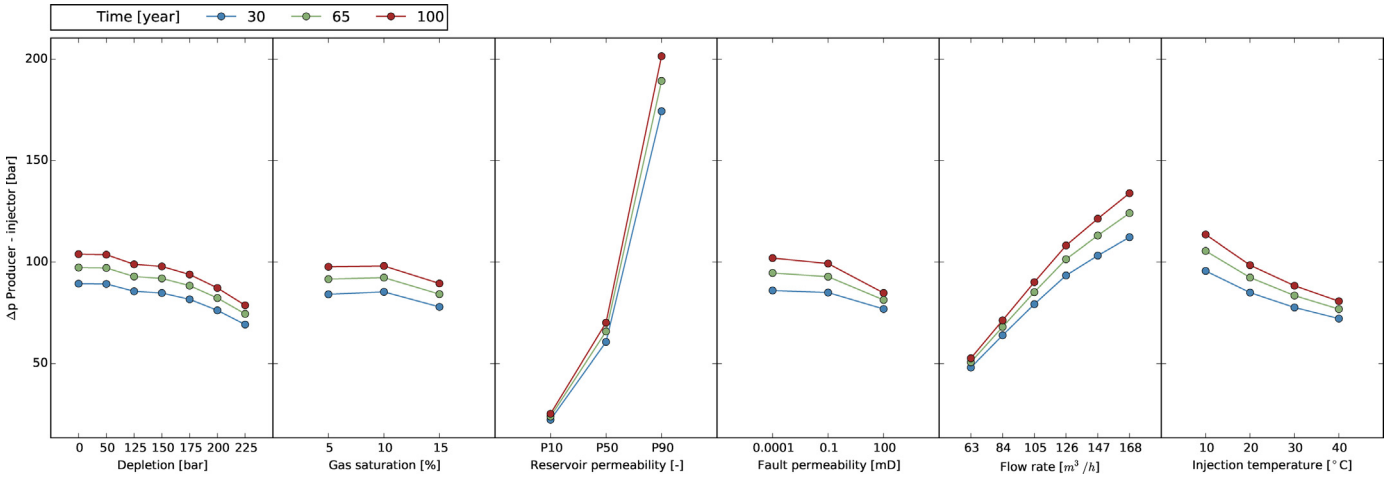

Fig. 12. Mean values of Δp between injector and producer for all uncertainty classes. Variable co-dependency causes the mean values presented to be different (lower) than the absolute values of the individual simulations presented in Fig. 11.

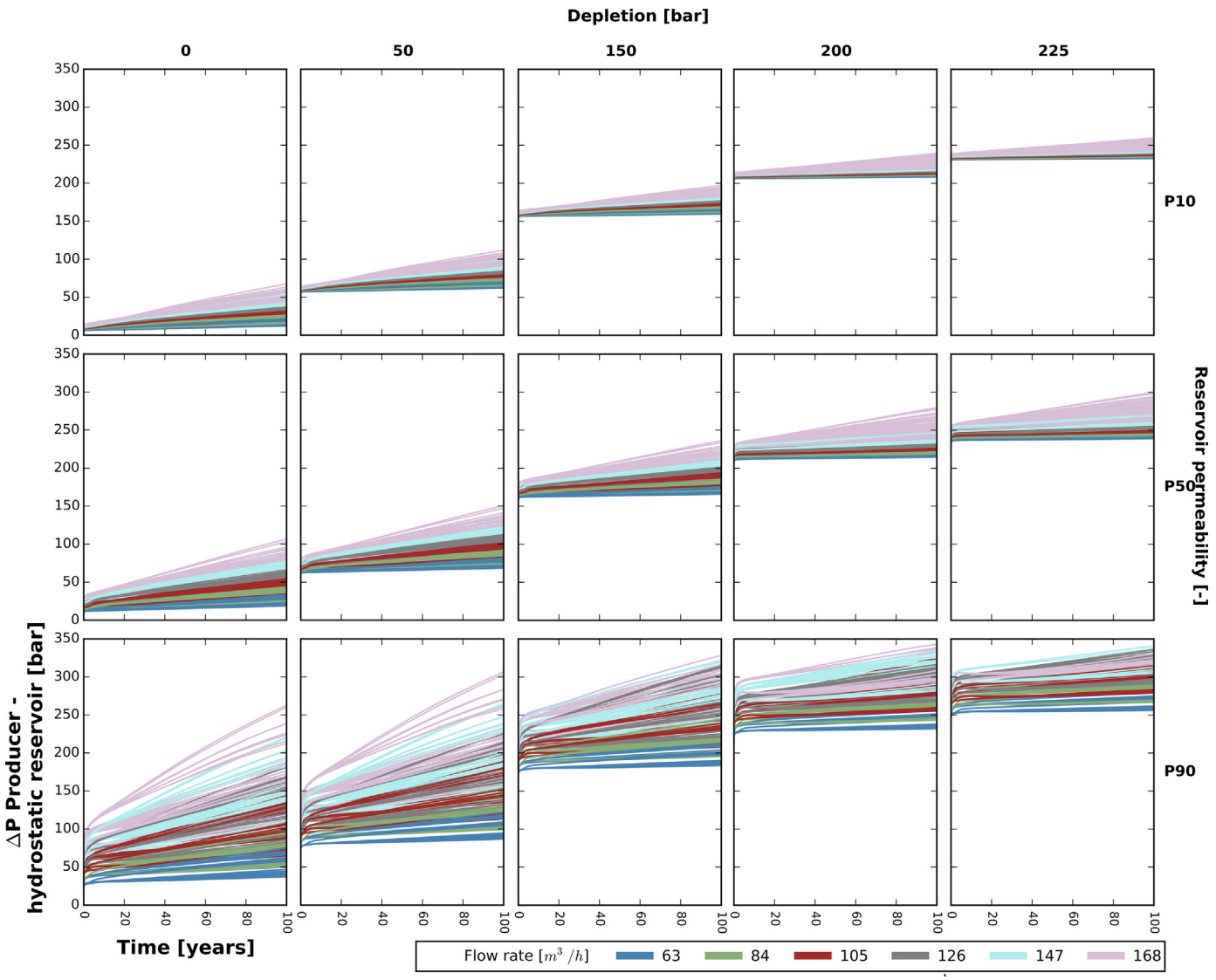

Fig. 13. Pressure difference between producer and hydrostatic reservoir pressure (no depletion). The pressure values represent the pumping pressure needed in the producer for the water to reach the surface. The lowest value in each subplot represents the equivalent depth at which the pump needs to be installed.

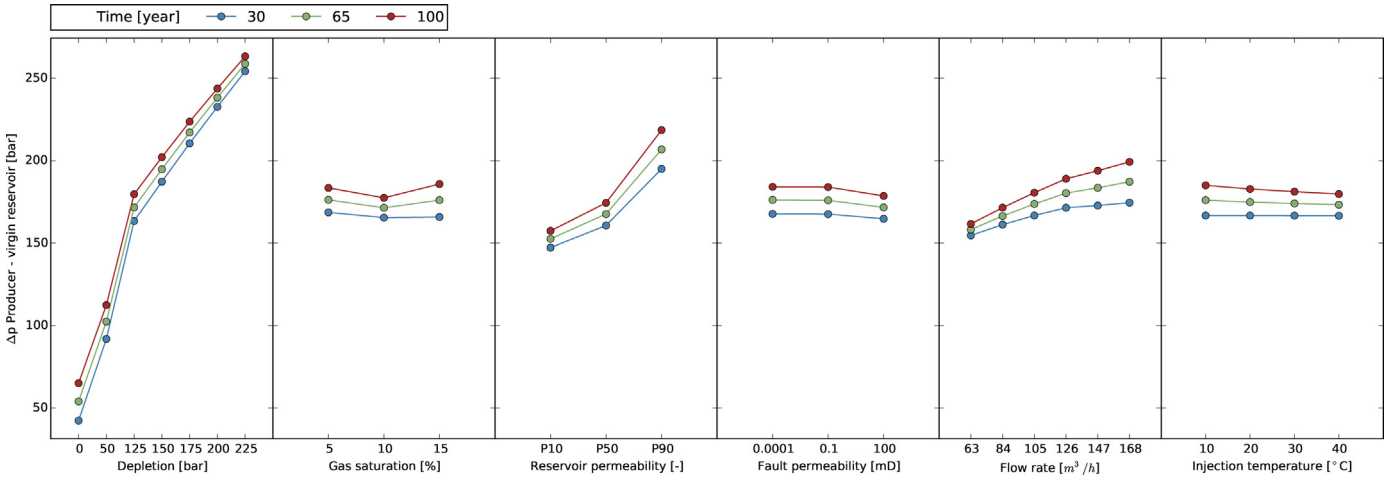

Fig. 14. Mean values of Δp between producer and hydrostatic reservoir (360 bar) for all uncertainty classes. The pressure difference values in the graph represent the hydraulic head that a producer pump would need to overcome.

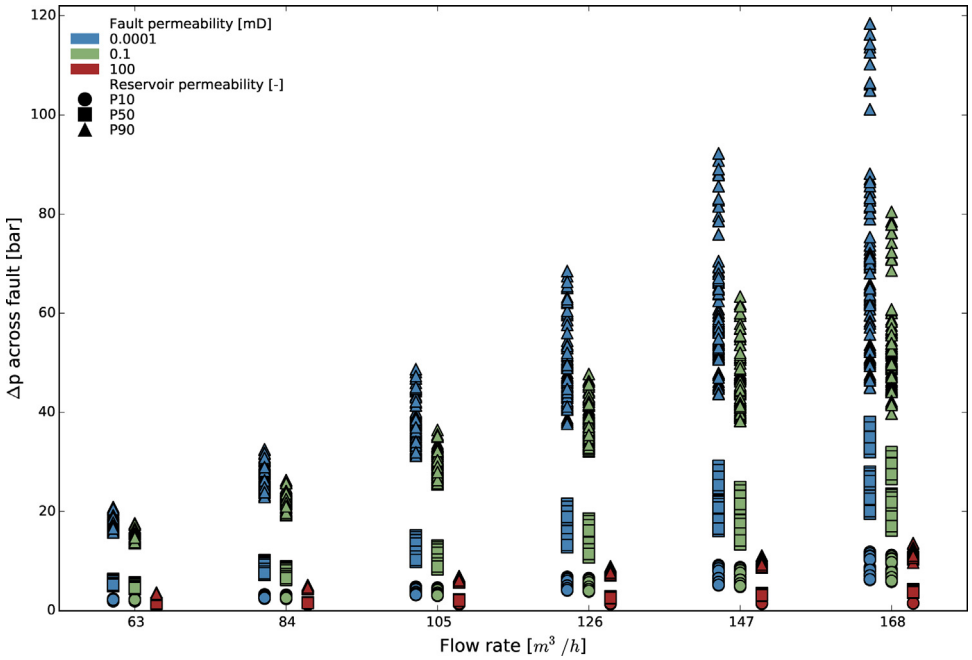

Fig. 15. Maximum Δp across fault against flow rate. Higher flow rate increases the range of maximum Δp. The effect is smaller for permeable faults and significantly higher for medium and low permeability faults. Reservoir permeability further amplifies this effect with higher permeability values leading to higher pressure values for the same flow rate. The spread becomes smaller for lower permeability values, but remains controlled by reservoir permeability. Data shown are from the cell pair across the fault surface that exhibits the highest Δp after 100 years of simulation.

the producer exhibits an as much as possible vertical trajectory. The surface location was fixed, based on preliminary arrangements made by the project. Since the focus of this work is on the reservoir, only the well trajectories in terms of downhole targets and deviations were considered in the model. Distance between producer and injector at reservoir depth is ca. 1250 m to ensure the desired doublet power output is met.

3.2.4. Geological modelling

The geological model includes the full stratigraphic interval from the top Rotliegend (ROCLT) to the base Saalian unconformity (Fig. 5). The Rotliegend dips towards the W-SW with an average inclination of 7% (Fig. 4). The top and base markers were interpreted from seismic together with the interface between the Silverpit formation (Ten Boer member—ROCLT) and the Slochteren members (ROSL) of the upper Rotliegend. The seismic signature of individual members within the reservoir is either too weak or not spatially continuous enough to allow 3D interpretation. Therefore the weighted gross thickness of the petrophysical layers was converted to thickness percentage based on the interpreted variable thickness of the Rotliegend sandstone. It should be noted that the ROCLT layer of the reservoir is not perforated in the simulations.

3.3. 3D reservoir model

All surfaces were imported directly from the geological model. Nevertheless, the juxtaposition of the layers across faults is not maintained in the reservoir model since PetraSim cannot accommodate this. The initial state model domain is 4.85 km by 2.25 km, in a depth range of ca. 2.9 km to ca. 3.9 km (Fig. 6). An overview of the inputs is depicted in Table 1. The horizontal cell dimension is 50 m × 50 m, while the vertical one is different for each stratigraphic zone, ranging between 24 m and 59 m (Table 2), which results in a total model size of 47,520 cells. The two major faults which bound the block (Fig. 4) were incorporated in the model with a vertical geometry. Fault horizontal resolution was 50 m × 50 m to account for the fault influence zone and interpretation uncertainty. The discretization allowed efficient simulation times, while retaining the resolution of the geological model as high as possible. Additionally, this setup is able to accommodate all the different time-steps for the range of parameter values (presented in the next chapters) without causing model disruptions or unreasonable simulation time. In this way all presented results make use of the same mesh specifications and are therefore cross comparable.

The generalized initial state is computed based on the pressure and temperature gradients for the study area. All other initial state models are based on this version. Following this, the initial state for each pressure depletion and gas saturation scenario was computed for a 100 years period using a fixed pressure and temperature boundary at the interface between the Rotliegend reservoir and the overlying Zechstein salt. The fixed boundary allowed for the modelling of the pressure depletion values.

A geothermal gradient of 31.3 °C/km (Bonté et al., 2012) (see also Appendix A) was used throughout the model, and a pressure gradient of 0.1 bar/m for the domain above the reservoir (surface to base Zechstein). The brine in the overburden has a salt mass fraction ratio of 0.03 and a very low gas saturation (1%.) For the reservoir part, nearby field data values indicated a NaCl concentration of 250,000 ppm (Bolourinejad and Herber, 2015), translating into a mass fraction of 17.31%.

4. Uncertainty & PyTOUGH automating

Each initial state model consists of a combination of values for pressure depletion and gas saturation (21 versions). The initial state model is further diversified using a unique combination of the reservoir and fault permeability, flow-rate and re-injection temperature values. The set of all possible variations for the given initial state constitutes a batch (Fig. 7).

Due to the number of simulations needed to capture the uncertainty, the handling of the input and result files had to be automated (Fig. 7). The initial state (pressure depletion and gas saturation) for each simulation batch was prepared separately and inspected in PetraSim. After the initial state was prepared, the remaining

Table 2
Reservoir layer characteristics of the Rotliegend Slochteren members (ROSL). Grouping the permeability values in P90-P50-P10 scenarios, the permeability range of influence is taken into account as a worst-middle-best estimation, based on the petrophysical data presented. Any combination of heterogeneity between or distribution within the layers, should fall within the range of these scenarios. Consequently, capturing further lateral permeability heterogeneity would not help to further differentiate between the range of permeability uncertainty influence and other uncertainty classes considered in the analysis.

Reservoir Layer	Vertical thickness	Porosity (%)	Permeability (mD)		
(top to base)	(m, avg)		P90	P50	P10
7	59	17.4	1	2	9
6	30	18.5	15	48	152
5	34	17.7	14	44	140
4	44	19.5	14	46	153
3	24	17.5	11	35	114
2	32	18.3	3	11	42
1	25	14.9	4	15	48

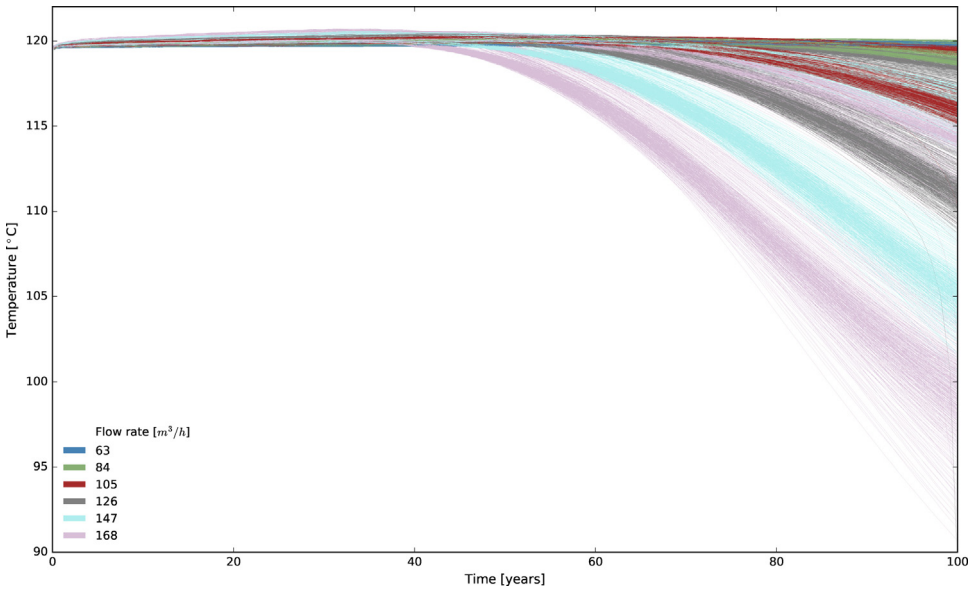

Fig. 16. Producer well temperature data for all 4377 simulation scenarios. Temperature drops by 10% of the initial production temperature only after around 75 years of simulation. A drop in produced water is not observed in any case before 45 years of production. Breakthrough time is not a significant parameter for the operations design.

parameters were automated using PyTOUGH scripts. The flow rate for both injector and producer was kept constant throughout the simulations. Simulation time was 100 years for all instances.

The first two classes (i.e. initial state and geological uncertainty) aim at capturing the uncertainties related to the reservoir conditions and properties, while the last one (operating uncertainty) evaluates the effect of possible development scenarios of the reservoir. All combinations of the discrete values were considered, amounting to 4536 unique full reservoir simulation runs. Data and graphs presented hereafter include all combinations of discrete values for all classes.

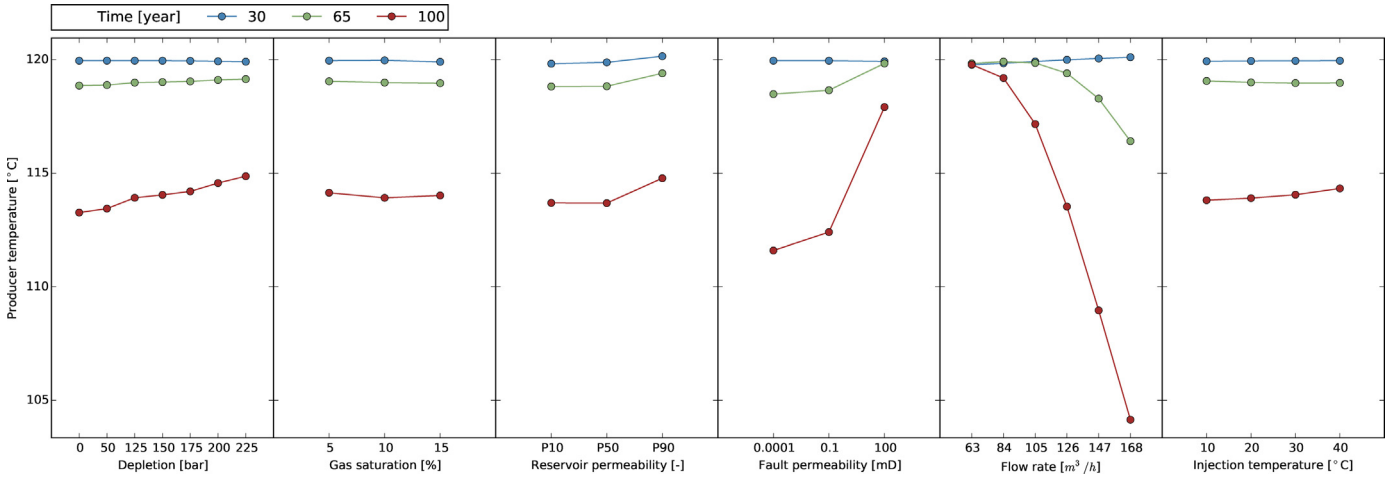

Fig. 17. Mean values of producer temperature for all uncertainty classes.

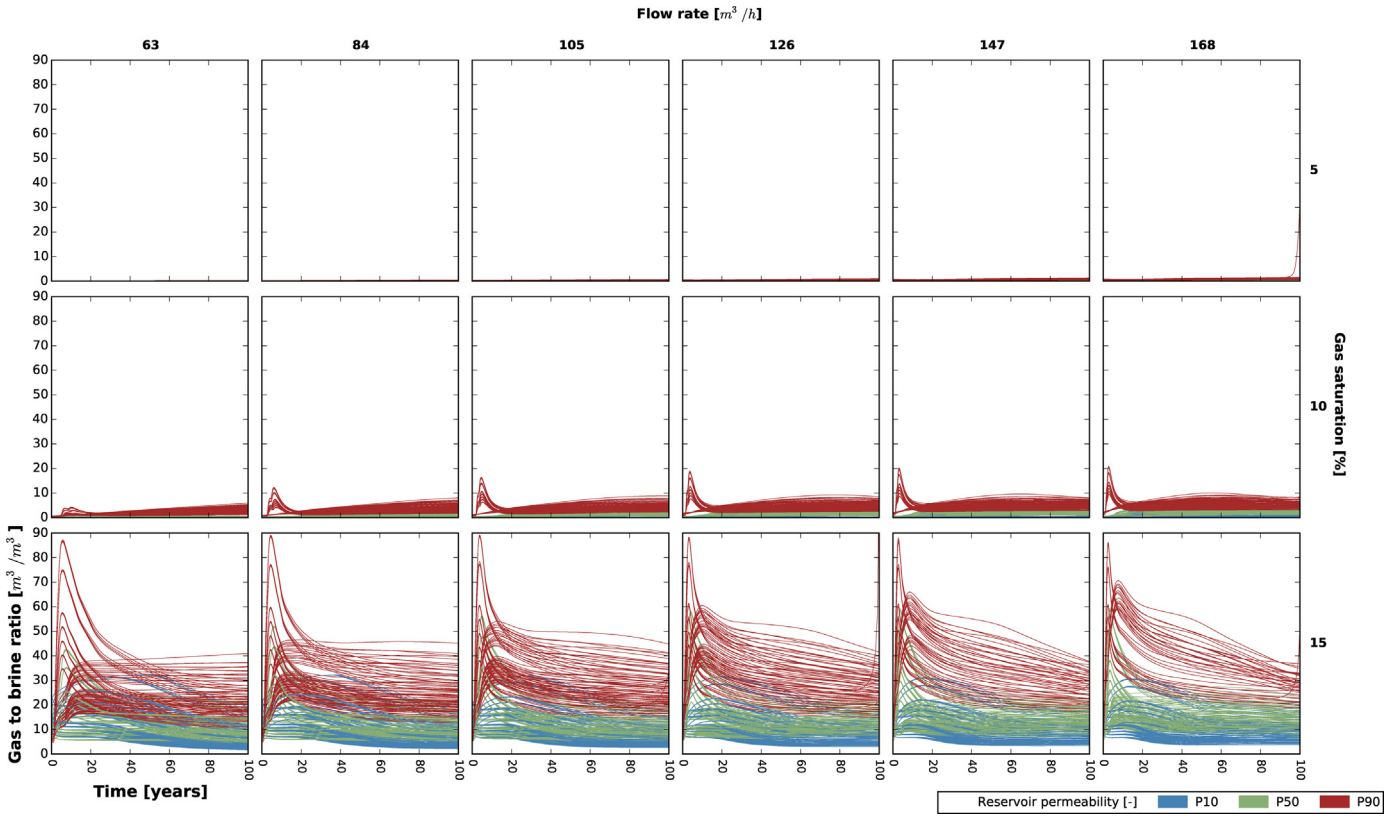

Fig. 18. Amount of gas m3 produced for every m3 of water at surface conditions. Gas saturation has a major effect and more gas is produced at higher initial gas saturation. Production further increases with higher flow rates. The effect of permeability is relatively low for lower saturations but becomes more significant with higher flow rates and gas saturations.

Different initial conditions were applied to the two domains (inside the Rotliegend reservoir and above it) to accommodate the pressure depletion scenarios. After the batch initial state is computed the fixed boundary (pressure and temperature) was removed so that pressure and temperature interactions could take place between reservoir and overburden. Within the reservoir, pressure depletion scenarios were accommodated by using the same gradient as the generalized initial state and a fixed value × for pressure depletion according to the formula Pressure = Z (X-0.1 bar/Z) (Z in m). Gas saturation in the reservoir was assigned three discrete values depending on the scenario, namely 5%, 10% and 15%.

Reservoir permeability values were arranged in three scenarios, namely P90, P50 and P10. The values are assigned discretely per layer based on the petrophysical data as detailed in Table 2 and chapter 3.2.2. Petrophysical data. Fault characteristics are divided in three scenarios consisting of a sealing, transparent and conduit behaviour to flow. These scenarios contained three discrete values for fault permeability (i.e. 0.0001, 0.1 and 100 mD). Six discrete values were considered for the flow rate covering a range between 63 and 168 m^3/h. Lastly, four re-injection temperature values were considered namely 10 °C, 20 °C, 30 °C and 40 °C.

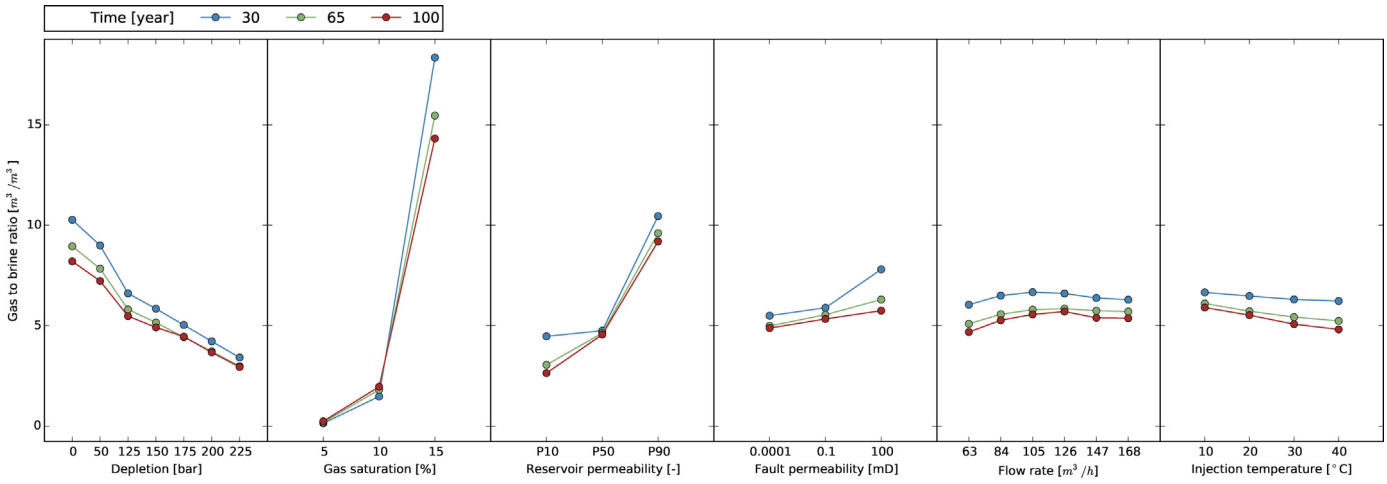

Fig. 19. Mean values for gas to brine ratio for all uncertainty classes.

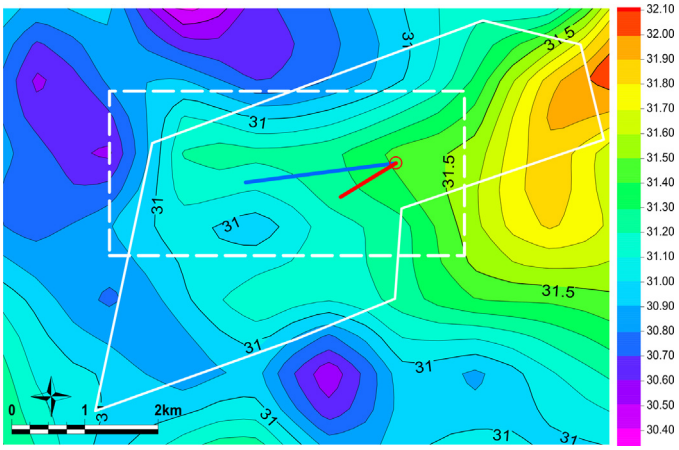

Fig. 20. Temperature gradient calculated using the NAM temperature top Rotliegend temperature and the interpreted depth. A surface temperature of 10 °C is used. The dotted line outlines the extent of the reservoir model, while the continuous line the extent of the Groningen license.

5. Results

Model output is subdivided in four main categories: power, pressure, temperature and gas content. These constitute the major areas of interest towards a project realization, revealing the effects of the uncertainty levels on performance and operation as well as in terms of field management. Data from all parameters are depicted in the graphs and together with the sensitivity plots, help to classify the most influential inputs. A small number (159 or 0.035%) of the simulations did not complete successfully (for details see Appendix B). Result data are compiled from the 4377 completed simulations.

5.1. Power

The thermal power output of the doublet is mostly controlled by the flow rate (Fig. 8). This is supported by previous researchers (Saeid et al., 2015). The flow rate controlled range of the thermal power output amounts to about +/− 1MW. Differences smaller than 1 MW are controlled by the remaining parameters (i.e. pressure depletion, gas saturation and re-injection temperature).

The effect of the re-injection temperature remains important, as the extracted power is always the difference between output and input of power. For the same flow rate, reducing the re-injection temperature results in a power output increase in steps of 0.5 MW to 2MW. Higher flow rate levels result in higher increases caused by reducing the re-injection temperature (Fig. 8). This relationship creates a counterbalance between flow rate and re-injection temperature. The same power can be extracted by simultaneously reducing the flow rate by one single step and increasing the re-injection temperature by 1.75–2.25 discrete steps. A thermal power of e.g. 10.5 MW can be generated with three different combinations of flow rata and re-injection temperature (84 m^3/h and 10 °C, 105 m^3/h and 30 °C and lastly 126 m^3/h and 40 °C respectively in the case of 100 mD fault permeability)

The effect of fault permeability becomes more pronounced over time (Fig. 8). More specifically, sealing faults reduce the affected reservoir volume and lead to an earlier drop in power. This effect is not distinguishable for flow rates up to 84 m^3/h. From there onwards it becomes increasingly more noticeable and appears to occur earlier in time for higher flow rates. For the highest considered flow rate, the effect of fault permeability is noticeable after 60 years and reduces the output by up to 6 MW, depending on the re-injection temperature.

It should be noted that although pressure depletion has no direct impact on the thermal power output of the reservoir, the reduced pressure implies that more energy will be needed for pumping, hence the net power output or Coefficient of Performance (CoP) will be lowered. Since pressure is a function of depth, the required pumping energy will be proportional to the amount of depletion. This could present technical limitations depending on the design specifications of the pump.

The mean output for each parameter group and respective inputs is depicted for some specified fixed times in Fig. 9. By computing the mean output of each parameter, the sensitivity of the thermal power to each of them is highlighted. It should be noted that since the parameter values are partly dependent and rather represent a set of combinations, the mean values do not capture the full range of power output as presented in Fig. 8.

The power output is mostly controlled by flow rate, which shows the highest spread in values. Over time the significance of flow rate is diminished, as can be seen from the 100 year data. Re-injection temperature reveals a fairly linear effect on power output which increases over time (30, 65 and 100 years). Nonetheless, the reduction of power output retains a linear relationship until the end of the simulation time. The temporal effect of fault permeability only becomes significant for lower permeability values.

The effect of both initial state parameters (pressure depletion and gas saturation) uncertainties are minor. The temporal effect on output increases, but seems unrelated to the discrete values of the parameters. The lower power output over time for initial state uncertainty can be explained by the other variables, most prominently flow rate.

5.2. Pressure

5.2.1. Power against Δp producer-injector

The pressure difference between producer and injector is indicative of the pumping energy that is required to extract the thermal power from the reservoir. The pressure difference between the wells is mostly controlled by the reservoir permeability, grouping the results in three discrete clusters (Fig. 10a & b). The evolving pressure difference at low reservoir permeability (P90) rises to very high values, up to 500 bar in some instances. For the P50 and P10 clusters this effect is much less pronounced. Within each cluster, a further grouping based on fault permeability can be observed. Lower permeability faults result in higher pressure differences, although the difference between 0.001 mD and 0.1 mD is not very pronounced, it is still discernible especially over a longer time period (Fig. 10b). This effect is enhanced at lower reservoir permeability values (P90). Consecutively, higher Δp values are observed, while the thermal power output decreases, especially for the high flow rates (Fig. 22b in Appendix C). Alternative cross-plots of the same datasets can be found in Appendix C.

5.2.2. Δp producer—injector

For lower reservoir permeability (P90) the pressure build up between injector and producer progresses slower but still increases significantly over time. Higher reservoir permeability values demonstrate proportionally faster pressure build up in the first simulation years, albeit with little increase over time. This mechanism seems to be mostly controlled by fault permeability, as a sealed reservoir compartment amplifies pressure development. At low reservoir permeability (P90), highest flow rate (168 m^3/h) and lowest fault permeability the minimum Δp at 100 years is just below 300 bar. Nonetheless, all reservoir permeability values exhibit a similar proportional increase of their minimum values with higher flow rates. Minimum values increase by a factor of approximately five between the lowest and the highest flow rate for the whole dataset.

Within the envelope defined by the flow rate, reservoir permeability and the temporal effect of the faults, further differentiation is invoked by the remaining parameters (depletion, gas saturation and re-injection temperature). The sensitivity of output values to variation in these input parameters is depicted in Fig. 12. The major influencing factor is reservoir permeability followed by flow rate, as was also evident from the individual simulation results (Fig. 11). These are closely followed by injection temperature. Over time the lower injection temperature values have an increasing effect on the Δp. Pressure depletion and gas saturation follow the same trend. Lastly, the effect of fault permeability is smaller in high permeability faults as pressure is not built up along fault surfaces over time.

5.2.3. Pressure difference between producer and hydrostatic reservoir pressure

Pressure depletion in the aquifer has a strong effect on the performance of the geothermal doublet, since it determines the pumping power required to bring the water to the surface. This is analysed with the help of Fig. 13 for a series of depletion scenarios. Using an average pressure of 360 bar (hydrostatic pressure level at the average reservoir depth), the Δp between the producer and the hydrostatic reservoir pressure can be computed (Fig. 13). The absolute pressure values are controlled by the degree of depletion in the aquifer due to nearby gas production in the Groningen field. The flow rate level controls a smaller range for each subplot as the depletion levels increase. The effect of reservoir permeability is a bit more complex. High and medium reservoir permeability values (P10 and P50 respectively) result in a smaller pressure envelope with a clear stratification based on the flow rate. Low reservoir permeability values (P90) result in a much broader envelope with higher absolute pressure values and significant overlap between the different flow rates. Furthermore, low reservoir permeability increases the pressure drop for the same flow rate, due to the resistance to flow within the reservoir. This results to higher minimum and maximum (increase of both) values per subplot.

The sensitivity of the Δp between the producer and hydrostatic reservoir clearly demonstrates the dominance of pressure depletion (Fig. 14). Reservoir permeability appears to be the second most influential factor with lower values leading to higher pressures. The effect of flow rate is also pronounced, further causing an increasing Δp over time. The remaining parameters of gas saturation, fault permeability and injection temperature have a minor effect.

5.2.4. Pressure across the fault plane

The maximum pressure build up along a fault surface is presented in Fig. 15. The data show the pressure development between the reservoir compartment and the juxtaposed fault block. The pressure levels are controlled by the combination of flow rate and reservoir permeability. The flow rate has a smaller effect on pressure development for high permeable faults, becoming stronger at lower fault permeabilities. Maximum values increase by a factor 3 for high fault permeability, a factor 4 for medium fault permeability and a factor 6 for low fault permeability. The range of pressures across the fault plane is clustered according to reservoir permeability. Higher differences between reservoir and fault permeability lead to an increased pressure difference.

5.3. Temperature

The producer well temperature is indicative of the rate at which the field is depleted of thermal energy. The producer temperature for all 4536 simulations is depicted in Fig. 16. No temperature decrease is observed before 45 years of simulation. Past 45 years, the temperature drops for the higher flow rate simulations. Nonetheless the temperature only drops by about 5 °C around 60 years of production and remains higher than 100 °C even after 80 years.

The slight temperature increase over 120 °C that is observed between years five and forty can be attributed to the additional input of deeper lying layers to the producer well (see Table 2). These layers have a lower permeability hence the flow through them starts to communicate to the producer at a latter state in time.

As observed from the producer temperature values displayed in Fig. 17, the temperature doesn't deviate from the initial value of ca. 120 °C during the first 30 years of simulation and is not affected by any of the parameters. At year 65 flow rate has the highest impact, while most other parameters, such as re-injection temperature have little to no effect. An exception is the high fault

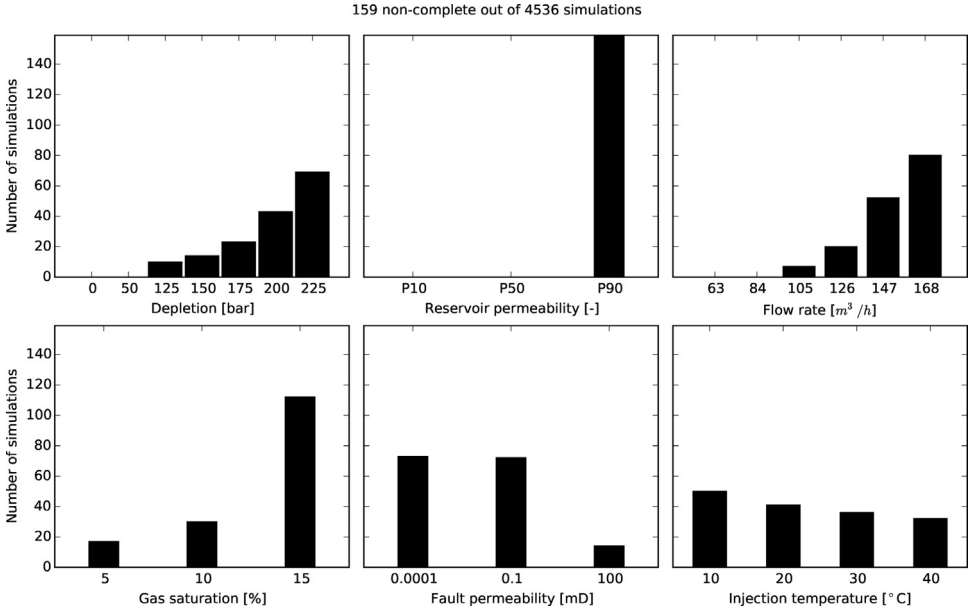

Fig. 21. Simulations that have not completed the full simulation time of 100 years amount to a total of 159 (0.035% of the total 4536). It should be noted that the numbers in the subplots are not cumulative. Each subplot amounts to 159, as a single simulation has a value for each parameter.

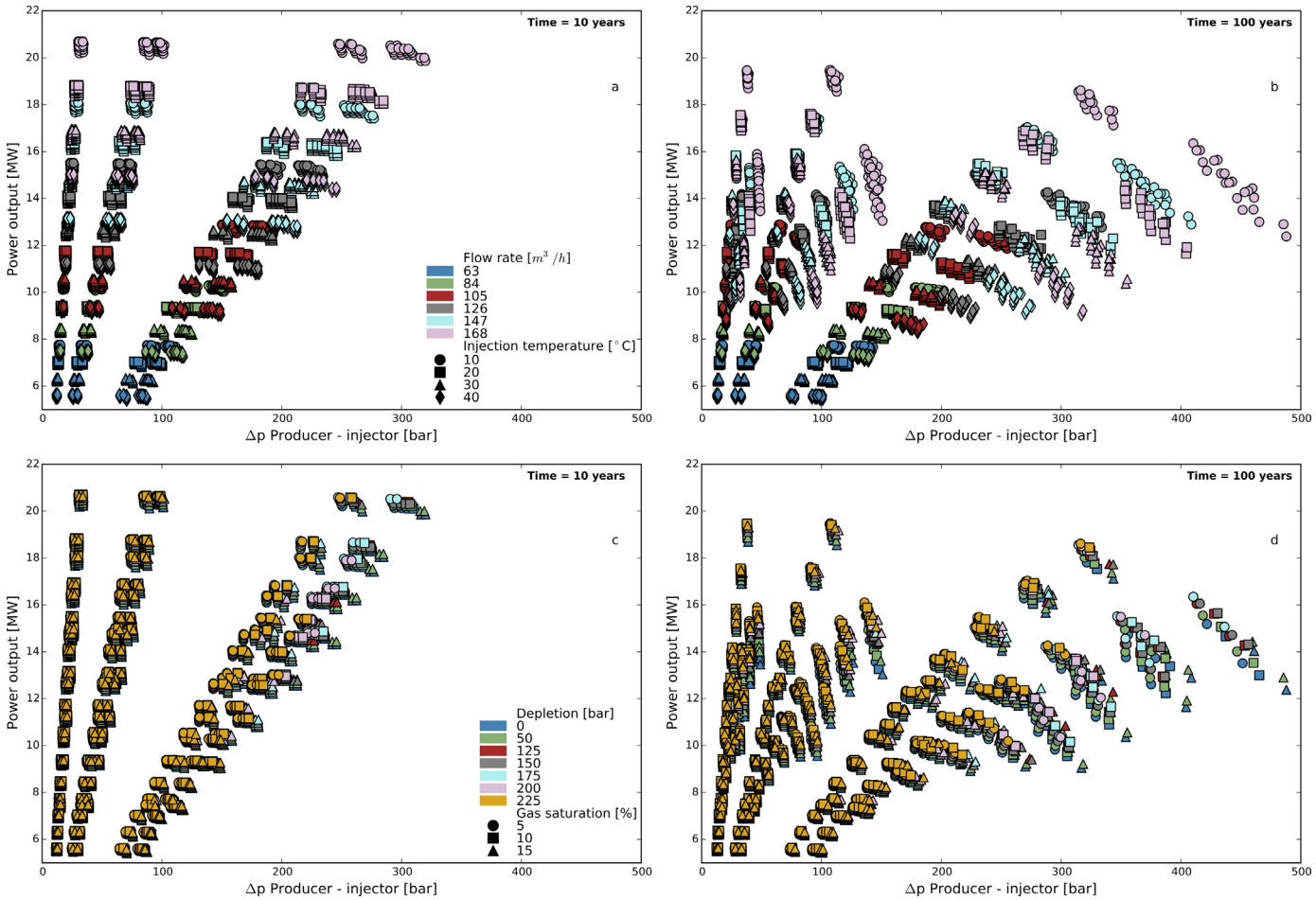

Fig. 22. Power output plotted against producer and injector Δp. but coded based on operational (a & b for 10 and 100 years respectively) and initial state uncertainty (c & d for 10 and 100 years respectively).

permeability that shows a positive effect, i.e. it does not lead to a temperature drop. After 100 years of simulation, flow rate remains the dominant parameter. High permeability faults do not contain the flow inside the faulted compartment, therefore the rock volume connected to the producer is larger and temperature remains high for a longer period of time. Over time hydrostatic reservoir pressure reduces the temperature slightly more than strong pressure depletion. Reservoir permeability does not seem to significantly affect the producer water temperature. Lastly, gas saturation and injection temperature seem to have almost no effect to the produced water temperature even after 100 years of simulation.

5.4. Gas

Gas production is usually reported in m^3 per day, but for geothermal applications, co-production of gas is more commonly referred to in terms of gas to brine ratio at surface conditions (Fig. 18). Within the range of parameters used in this analysis, the gas production in this setting varies between close to zero and almost 90 m^3/m^3.

The spike on the all graphs within the first ten simulation years can be attributed to the pressure front from the injector reaching the producer and displacing the gas. This is followed by a drop in gas production which stabilizes over time. Low initial gas saturation leads to minor amounts of gas at the producer well. For the middle and high initial gas saturation (10% and 15% respectively) there is a clear ordering, with lower reservoir permeability (P90) generally leading to higher gas production. Lower reservoir permeability results in a higher gas to brine ratio through the increase of absolute permeability of the gaseous phase as described by the Klinkenberg effect (Tanikawa and Shimamoto, 2009) which is included in the TOUGH2 code (Pruess et al., 2012). As reservoir permeability increases (P50 and P10), smaller amounts of gas are produced and the gas is not displaced as effectively.

Based on the results of the sensitivity analysis (Fig. 19), the production of gas seems to be the most complex component. Even though the produced gas to brine ratio is dominated by the initial gas saturation, all parameters affect this ratio. The degree of depletion is also crucial, since at a given gas saturation at reservoir level, it determines the volume of the gas at reservoir conditions as well as the expansion factor when the gas is transferred to standard conditions at the surface. Higher reservoir pressure depletion therefore progressively leads to a lower ratio of gas being produced. Low reservoir permeability values help the displacement and production of gas significantly more than medium and high values. High fault permeability also results in higher gas to brine ratios, but over time this effect is minimized. Flow rate has a modest increasing effect up to 126 m^3/h, after which a lowering and plateau is observed. Lastly, high injection temperature decreases the amount of produced gas over time, while lower injection temperatures cause a smaller reduction.

6. Discussion

Uncertainty of the parameters determining the initial state of reservoir and porefill has the largest impact on pressure output

Table 3
Risk assessment overview through the effect of uncertainty parameters to simulation output.

			Output impact			
		Thermal power (MW)	Δp producer–injector (bar)	Δp producer–hydrostatic reservoir (bar)	Producer temperature (°C)	Gas to brine ratio (m^3/m^3)
Uncertainty parameter	Depletion [bar]	low	low	high	low	medium
	Gas saturation [%]	low	low	low	low	high
	Reservoir permeability [–]	low	high	medium	low	medium
	Fault permeability [mD]	low (temporal)	low	low	medium (temporal)	medium-low
	Flow rate [m^3/h]	high	high	medium	high	low
	Injection temperature [°C]	medium	medium	low	low	low

between well and reservoir, as well as the amounts of gas produced. More specifically, *pressure depletion* in the reservoir is most influential to the Δp between the producer well and a hypothetical undisturbed reservoir pressure level (Fig. 14). This effectively controls the depth at which the production pump needs to be installed and may have further implications regarding well trajectory. The producer well trajectory used in this study was designed to accommodate some level of pressure depletion, by means of a vertical hole (down to 2500 m) to allow for the pump installation. Spatial restrictions apply to the surface location of the wells, the optimal target at depth and the extent of the concession which limits the drainage area. Pressure depletion further constricts the installation design. Additionally, the deeper installation of the production pump complicates its design characteristics and even project feasibility. Furthermore, the reported Δp here might even be higher when a finer mesh is used in the model around the wells to better capture near wellbore effects and the dynamic level of the water table. It should be noted that if pressure depletion is present in the aquifer, it will progress during the production period (Van Wees et al., 2014) since the causal mechanism (gas production in the neighbouring gas field) is still active. Thus, the evolution of the pressure depletion levels in time in relation to geothermal energy production requires further investigation.

Uncertainty of the level of *gas saturation* in the reservoir has a dominant effect on the produced gas to brine ratio. A high gas to brine ratio could serve as an additional energy and income source for a geothermal project (van Heekeren and Bakema, 2015). Simultaneously, the presence of gas can further complicate the technical feasibility of the pump installation (i.e. gas coming out of solution) and the surface facilities (Frick et al., 2011; van Heekeren and Bakema, 2015).

Geological uncertainty pertains mostly to pressure output and secondly to gas production levels and thermal and temperature output. Thermal power seems to be the least affected. *Reservoir permeability* dominates the Δp between the wells. It further determines the pumping energy needed to extract a certain amount of energy. The extremely high pressure resulting from low reservoir permeability will significantly reduce the CoP. Nonetheless, limitations related to low reservoir permeability could be offset by hydraulic stimulation as has been demonstrated in Rotliegend sediments at the Groß Schönebeck field (Legarth et al., 2005; Zimmermann and Reinicke, 2010) or by a hybrid system between the two versions of natural and stimulated reservoir (Blöcher et al., 2015). Alternatively, a different perforation scheme could selectively target the layers with better flow characteristics.

Fault permeability has a medium to low temporal effect on the producer well temperature and thermal power, but it does further affect the gas to brine ratio. Effectively, the presence and permeability of faults influence the fluid volume connected to the producer well. Sealing faults alter both heat extraction and gas production on a temporal level by confining the volume and accelerating resource depletion. This effect highlights the importance of 3D geometric reservoir modelling, as this aspect would have been overlooked using a more simplified 2D model. Furthermore the inclusion of the faults themselves allows examining the pressure front development around them. This aspect remains highly pertinent as induced seismicity relates closely to existing faults (Van Wees et al., 2014). The relevance of this is important since high overpressures (>200 bar) are present in the Lauwerszee Trough (Verweij et al., 2011). Results presented in Fig. 15 do not constitute an exhaustive analysis of the effect of pressure on faults. In-situ mechanical stress and full fault geometry need to be part of the analysis to provide a broad understanding of the interrelation between fluid injection and seismic activity (Moeck et al., 2009). Earthquakes in sedimentary geothermal settings have been documented to be negligible in magnitude (Evans et al., 2012). However, cyclic production could also aid to mitigate the pressure build up, allowing for pressure redistribution within the reservoir, thus reducing Δp across faults. Still, this project involves a more complex geological setting where advancing pressure depletion and geothermal production might lead to different results. For this purpose further input is needed, as well as different meshing and simulating tools that can better handle complex fault geometry. Nonetheless, this highlights a crucial point for geothermal development and a parameter which needs to be considered as a starting point for a comprehensive analysis of the effects of geothermal energy production on fault behaviour.

Operational uncertainty has an important influence on most outputs with the exception of gas to brine ratio. *Flow rate levels* govern thermal power, producer temperature and doublet pressure difference. There is however a certain degree of freedom which allows a trade-off, such that the same power output can be achieved through more than one combination of flow rate levels and re-injection temperatures. This finding is supported by similar outcomes for geothermal power plants (Franco and Villani, 2009). Since direct use of geothermal heat does not operate under the optimized and fine-tuned conditions needed for binary electricity plants (Franco and Villani, 2009), this trade-off becomes more valuable. Flow rate still remains important for pressure differences between producer and hydrostatic reservoir. Nonetheless, this aspect needs further research since the applied mesh resolution might underestimate the pressure levels in close proximity to the wells and the difference between static and dynamic fluid level (Frick et al., 2011).

The *reinjection temperature* indirectly controls the amount of extracted heat from the reservoir and is the second most important parameter determining doublet power; this is most notable in

the temporal dimension and corroborates previous analytical findings (van Wees et al., 2012). This aspect strongly dictates the mode of operation, as well as the design of surface facilities and should be considered when deciding on the size of the doublet. Reinjection temperature does not significantly shorten project life since the first effects are observed only after 60 years in the worst case. Pressure difference between producer and injector is only affected moderately by the reinjection temperature, relating to density and viscosity differences caused by temperature (Francke and Thorade, 2010).

The applied workflow enables the establishment of a comprehensive risk matrix (Table 3) with regard to the three uncertainty levels discussed (initial state, geological and operational). The input levels, value ranges and outputs presented in this analysis constitute an extension of previously considered uncertainties. More significantly, the parameter co-dependency demonstrates the relative importance of each input to the different analysis outputs. The assessment can serve as starting point to identify critical project aspects and steer the focus of further research needed prior to drilling the exploration well. The breadth of the analysis is underpinned by 3D field geometry and 3D numerical reservoir simulations and can therefore support both quantitative as well as qualitative insights.

The methodology can be further expanded to include other parameters or broader value range of uncertainty where appropriate. The number of simulations however would increase dramatically. The ensemble of 4536 simulations highlights that uncertainties still remain, even in a mature hydrocarbon basin with a wealth of available subsurface data. Decisions on doublet sizing or data and engineering requirements can decrease the uncertainty range included in the analysis before the applied methodology, thereby reducing the number of simulations needed. The proposed workflow can contribute to risk comprehension and lead to more successful implementation of direct use geothermal projects.

The number of parameters and their co-dependent arrangement create a six dimensional solution space on top of the four dimensions of reservoir simulation. The difficulty to visualize these data can be circumvented through the sensitivity analysis that highlights the relative importance of the parameters. In the absence of available data, a careful selection of the parameters and their values can still generate useful results and insights through the same mechanism. This widens the applicability of the paradigm presented.

Some limitations of the study are still relevant. Retaining the geological model resolution to the reservoir simulator was suboptimal. The added definition especially related to fault geometry could further fine-tune the findings. Furthermore, the complexity of the workflow highlights the need for integrated geothermal assessment tools.

7. Conclusion

The employed methodology results in a comprehensive reservoir risk assessment of a geothermal direct use installation. Three levels of uncertainty are included in the discrete parameter analysis, namely initial state, geological and operational uncertainty. The analysis is based on a 3D geological model and is carried out through an ensemble of 4536 unique numerical 3D reservoir simulations extending over 100 simulation years. All possible combinations of the discrete parameters are considered. The relative effect of each parameter class is extracted by means of a sensitivity analysis. A risk assessment matrix provides a qualitative overview, while the wealth of generated data deliver quantitative output ranges. While the methodology is transferable to other geothermal fields, the numerical results are restricted to the Groningen concession.

Making use of available data and uncertainty ranges with the methodology, we conclude that the thermal energy in the envisioned Groningen geothermal doublet (Rotliegend reservoir) can be sustained beyond 60 years (5 °C temperature drop) under all simulations.

Regarding initial state uncertainty, pressure depletion can significantly affect the production pump installation depth. A pressure head of up to 325 bar could be required by the pump, resulting in major technical challenges. Therefore, reservoir pressure depletion is a major risk for geothermal projects. Reservoir gas saturation levels control the amount of gas that might be co-produced. Volumes of up to 90 m^3 of methane per m^3 of produced brine can be expected for a gas saturation of 15%.

Pressure difference within the reservoir is controlled by reservoir permeability. Low permeability (P90) can generate pressure differences up to 500 bar, while medium permeability (P50) only reaches up to 150 bar. Fault permeability, the second geological uncertainty parameter, affects the produced water temperature. Sealing faults start to affect the produced temperature after 60 years of simulation time.

Operational uncertainty parameters present trade-offs between them and the same power output can be achieved with more than one flow rate and re-injection temperature combinations. Flow rate impacts both pressure and the thermal power outputs significantly. The Groningen geothermal doublet can produce power in excess of 21 MW at the pressure penalty of up to 300 bar. Additionally, injection temperature impacts power output and pressure. For the same flow rate up to 5 MW more can be extracted by reducing the injection temperature from 40 °C to 10 °C.

Acknowledgements

This research was supported by the research grant Flexiheat (Ministerie van Economische Zaken, Landbouw en Innovatie). The authors would further like to acknowledge Nederlandse Aardolie Maatschappij BV (NAM, a Shell operated 50-50 joint venture with ExxonMobil) for providing the 3D seismic data and Schlumberger for the academic Petrel license. We would also like to thank colleagues Herman van Os and Panteha Bolourinejad, as well as our anonymous reviewer for helping to improve this paper.

Appendix A

Temperature data for the top of the Rotliegend (Ten Boer formation) from a basin model in the Groningen area where available to us from NAM (NAM, 2015). The dataset makes use of borehole temperature data from the Groningen gas field and surrounding wells. Using the dataset a temperature gradient map was produced (Fig. 20). Assuming a temperature of 10 °C at the surface, the average temperature gradient around the concession is 31.3 °C/m which is in agreement with the dataset from literature (Bonté et al., 2012).

Appendix B. Non-complete simulations

Non-complete simulations

Some simulations have not completed due to very high pressures that cannot be accommodated by the TOUGH2 simulator. The crashed simulations and their respective input parameter values are presented in Fig. 21. All simulations that have not completed share low reservoir permeability values (P90). Higher values of depletion, gas saturation and flow rate show an increasing number of incomplete simulations. Opposite to this, higher fault permeability and injection temperature reduce the number of simulations that have not reached full simulation time. Since there is not a

clear physical reason why this might occur (though pressure built up is the most prominent one), crashed simulations do not necessarily mean that such scenarios cannot be realized. Nonetheless, the lower reservoir permeability values (P90) can be seen as an important factor for failure. Since all crashed simulations exhibit low reservoir permeability values, all abovementioned results have a more poorly represented effect of low permeability (P90).

Appendix C

The dataset depicted in Fig. 22 is identical to the one presented in Fig. 10. The effect of flow rate and injection temperature defines the clustering regarding the thermal power output (operational uncertainty parameters). This effect can be also followed on the temporal dimension, in Fig. 22b. The effect on pressure difference is not clear using this coding. The scatter patterns of the geological uncertainty do not allow for a meaningful interpretation of the results.

Appendix A. Supplementary data

Supplementary data associated with this article can be found, in the online version, at doi:10.1016/j.geothermics.2016.06.0141.

References

Battistelli, A., Calore, C., Pruess, K., 1997. The simulator TOUGH2/EWASG for modelling geothermal reservoirs with brines and non-condensible gas. Geothermics 26, 437–464.

Blöcher, G., Cacace, M., Reinsch, T., Watanabe, N., 2015. Evaluation of three exploitation concepts for a deep geothermal system in the North German Basin. Comput. Geosci. 82, 120–129.

Boersma, K., Brinkgreve, D., 2014. GRN-GT-01 & GRN-GT-02 detailed design 2.2, 1–87.

Bolourinejad, P., Herber, R., 2015. Experimental investigation of porosity and permeability variations in reservoirs and caprock following co-injection of sulfur dioxide and hydrogen sulfide with carbon dioxide. J . Pet. Sci. Eng. 129, 137–144.

Bonté, D., Van Wees, J.D., Verweij, J.M., 2012. Subsurface temperatureof the onshore Netherlands: new temperature dataset and modelling. Neth . J. Geosci. 91, 491–515.

Breunese, J.N., van Thienen-Visser, K., 2014. Effecten van verschillende productiescenario's op de verdeling van den compactie in het Groningen veld in de periode 2014 tot en met 2016 R10427, 1–29.

Carlson, M.R., 2003. Practical Reservoir Simulation: Using, Assessing, and Developing Results. PennWell Books.

Croucher, A., 2014. PyTOUGH user's guide 1.4.0, 1–99.

de Jager, J., Geluk, M.C., 2007. Petroleum Geology. In: Wong, T.E., Batjes, D.A.J., de Jager, J. (Eds.), Geology of the Netherlands. Royal Netherlands Academy of Arts and Sciences, Amsterdam, Netherlands, pp. 241–264.

de Jager, J., 2007. Geological development. In: Wong, T.E., Batjes, D.A.J., de Jager, J. (Eds.), Geology of the Netherlands. Royal Netherlands Academy of Arts and Sciences, Amsterdam, Netherlands, pp. 5–26.

Doornenbal, J.C., Abbink, O.A., Duin, E.J.T., Dusar, M., Hoth, P., Jasionowski, M., Lott, G.K., Mathiesen, A., Papiernik, B., Peryt, T.M., Veldkamp, J.G., Wirth, H., 2010. Introduction, stratigraphic framework and mapping. In: Doornenbal, J.C., Stevenson, A. (Eds.), Petroleum Geological Atlas of the Southern Permian Basin Area. EAGE Publications b.v., Houten, The Netherlands, pp. 1–9.

Evans, K.F., Zappone, A., Kraft, T., Deichmann, N., Moia, F., 2012. A survey of the induced seismic responses to fluid injection in geothermal and CO2 reservoirs in Europe. Geothermics 41, 30–54.

Florian Wellmann, J., Croucher, A., Regenauer-Lieb, K., 2012. Python scripting libraries for subsurface fluid and heat flow simulations with TOUGH2 and SHEMAT. Comput. Geosci. 43, 197–206.

Francke, H., Thorade, M., 2010. Density and viscosity of brine: An overview from a process engineers perspective. Chem. Erde Geochem. 70 (Suppl. 3), 23–32.

Franco, A., Vaccaro, M., 2014. Numerical simulation of geothermal reservoirs for the sustainable design of energy plants: a review. Renew. Sustain. Energy Rev. 30, 987–1002.

Franco, A., Villani, M., 2009. Optimal design of binary cycle power plants for water-dominated, medium-temperature geothermal fields. Geothermics 38, 379–391.

Frick, S., Regenspurg, S., Kranz, S., Milsch, H., Saadat, A., Francke, H., Brandt, W., Huenges, E., 2011. Geochemical and process engineering challenges for geothermal power generation. Chem. Ing. Tech. 83, 2093–2104.

Fryberger, S.G., Knight, R., Hern, C., Moscariello, A., Kabel, S., 2011. Rotliegend facies, sedimentary provinces, and stratigraphy, Southern Permian basin UK and The Netherlands: a review with new observations. In: Grötsch, J., Gaupp, R. (Eds.), The Permian Rotliegend of the Netherlands. SEPM (Society for Sedimentary Geology), Oklahoma, USA, pp. 51–88.

Grötsch, J., Sluijk, A., van Ojik, K., de Keijzer, M., Graaf, J., Steenbrink, J., 2011. The Groningen gas field: fifty years of exploration and gas production from a Permian dryland reservoir. In: Grötsch, J., Gaupp, R. (Eds.), The Permian Rotliegend of the Netherlands. SEPM (Society for Sedimentary Geology), Oklahoma, USA, pp. 11–33.

Henares, S., Bloemsma, M.R., Donselaar, M.E., Mijnlieff, H.F., Redjosentono, A.E., Veldkamp, H.G., Weltje, G.J., 2014. The role of detrital anhydrite in diagenesis of aeolian sandstones (Upper Rotliegend, The Netherlands): Implications for reservoir-quality prediction. Sediment. Geol. 314, 60–74.

Laier, T., Kockel, F., Geluk, M.C., Pokorsky, J., Milaczewski, L., Lott, G.K., 1997. Section A: geology. In: Lokhorst, A. (Ed.), Nw European Gas Atlas. Netherlands Institute of Applied Geoscience TNONational Geological Survey, Harlem, The Netherlands.

Legarth, B., Huenges, E., Zimmermann, G., 2005. Hydraulic fracturing in a sedimentary geothermal reservoir: results and implications. Int. J. Rock Mech. Min. Sci. 42, 1028–1041.

Leveille, G.P., Knipe, R., More, C., Ellis, D., Dudley, G., Jones, G., Fisher, Q.J., Allinson, G., 1997. 1. Compartmentalization of Rotliegendes gas reservoirs by sealing faults, Jupiter Fields area, southern North Sea, 123. Geological Society London, Special Publications, pp. 87–104.

Ligtenberg, H., Okkerman, J., de Keijzer, M., 2011. Fractures in the Dutch Rotliegend? An overview. In: Grötsch, J., Gaupp, R. (Eds.), The Permian Rotliegend of the Netherlands. SEPM (Society for Sedimentary Geology), Oklahoma, USA, pp. 229–244.

McKie, T., 2011. A comparison of modern dryland depositional systems with the Rotliegend group in the Netherlands. In: Grötsch, J., Gaupp, R. (Eds.), The Permian Rotliegend of the Netherlands. SEPM (Society for Sedimentary Geology), Oklahoma, USA, pp. 89–103.

Moeck, I., Kwiatek, G., Zimmermann, G., 2009. Slip tendency analysis, fault reactivation potential and induced seismicity in a deep geothermal reservoir. J. Struct. Geol. 31, 1174–1182.

Mottaghy, D., Pechnig, R., Vogt, C., 2011. The geothermal project Den Haag: 3D numerical models for temperature prediction and reservoir simulation. Geothermics 40, 199–210.

Muntendam-Bos, A.G., Wassing, B.B.T., Geel, C.R., Louh, M., Thienen-Visser, K., 2008. Burgemeer seismicity study 2008-U-R1071/B.

NAM, 2015. Personal communication: temperature map at the top of the Rotliegend in the area of the Groningen gas field.

NLOG, 2015. SAU-01 2015.

Ondrak, R., Wenderoth, F., Scheck, M., Bayer, U., 1998. Integrated geothermal modeling on different scales in the Northeast German basin. Geol. Rundsch. 87, 32–42.

Poulsen, S.E., Balling, N., Nielsen, S.B., 2015. A parametric study of the thermal recharge of low enthalpy geothermal reservoirs. Geothermics 53, 464–478.

Pruess, K., Oldenburg, C., Moridis, G., 2012. TOUGH2 User's Guide, Version 2.1 LBNL-43134.

Pruess, K., 1991. TOUGH2: A general-purpose numerical simulator for multiphase fluid and heat flow Report LBL-29400.

Rockware, 2014 PetraSim.

Saeid, S., Al-Khoury, R., Nick, H.M., Hicks, M.A., 2015. A prototype design model for deep low-enthalpy hydrothermal systems. Renew. Energy 77, 408–422.

Schön, J.H., 2011. Physical Properties of Rocks: A Workbook. Elsevier.

Schlumberger, 2012. Petrel 2012 Geology and modelling 12-IS-0333.

TNO, 2014. Toetsing van de bodemdalingsprognoses en seismische hazard ten gevolge van gaswinning van het Groningen veld Rl l953, 1–218.

Tanikawa, W., Shimamoto, T., 2009. Comparison of Klinkenberg-corrected gas permeability and water permeability in sedimentary rocks. Int. J. Rock Mech. Min. Sci. 46, 229–238.

van Gent, H.W., Back, S., Urai, J.L., Kukla, P.A., Reicherter, K., 2009. Paleostresses of the Groningen area, the Netherlands—results of a seismic based structural reconstruction. Tectonophysics 470, 147–161.

van Heekeren, V., Bakema, G., 2015. The Netherlands Country Update on Geothermal Energy, 1–6.

van Hulten, F.F.N., 2010. Geological Factors Effecting Compartmentalization of Rotliegend Gas Fields in the Netherlands, 347. Geological Society London, Special Publications, pp. 301–315.

van Leeuwen, L., Böker, U., van de Weerd, A., 2014. Geothermal Energy in Groningen Geological Investigation. Groot Geologisch Onderzoek Groningen) G1111, pp. 1–99.

van Ojik, K., Böhm, A.R., Cremer, H., Geluk, M.C., de Jong, M.G.G., Mijnlieff, H.F., Nio, S.D., 2011. The rationale for an integrated stratigraphic framework of the upper Rotliegend II depositional system in the Netherlands. In: Grötsch, J., Gaupp, R. (Eds.), The Permian Rotliegend of the Netherlands. SEPM (Society for Sedimentary Geology), Oklahoma, USA, pp. 37–48.

van Thienen-Visser, K., Breunese, J., 2015. Induced seismicity of the Groningen gas field: history and recent developments. Lead. Edge 34, 664–671.

van Wees, J.D., Kronimus, A., van Putten, M., Pluymaekers, M.P.D., Mijnlieff, H., van Hooff, P., Obdam, A., Kramers, L., 2012. Geothermal aquifer performance assessment for direct heat production—methodology and application to Rotliegend aquifers. Neth . J. Geosci. 91, 651.

Van Wees, J.D., Buijze, L., Van Thienen-Visser, K., Nepveu, M., Wassing, B.B.T., Orlic, B., Fokker, P.A., 2014. Geomechanics response and induced seismicity during gas field depletion in the Netherlands. Geothermics 52, 206–219.

Verweij, H., Simmelink, E., Underschultz, J., 2011. Pressure and fluid flow systems in the Permian Rotliegend in the Netherlands onshore and offshore. In: Grötsch, J., Gaupp, R. (Eds.), The Permian Rotliegend of the Netherlands. SEPM (Society for Sedimentary Geology), Oklahoma, USA, pp. 247–263.

Vogt, C., Mottaghy, D., Wolf, A., Rath, V., Pechnig, R., Clauser, C., 2010. Reducing temperature uncertainties by stochastic geothermal reservoir modelling. Geophys. J. Int. 181, 321–333.

Vogt, C., Iwanowski-Strahser, K., Marquart, G., Arnold, J., Mottaghy, D., Pechnig, R., Gnjezda, D., Clauser, C., 2013. Modeling contribution to risk assessment of thermal production power for geothermal reservoirs. Renew. Energy 53, 230–241.

Zimmermann, G., Reinicke, A., 2010. Hydraulic stimulation of a deep sandstone reservoir to develop an Enhanced Geothermal System: laboratory and field experiments. Geothermics 39, 70–77.